Lawrence Berkeley National Laboratory
LBL Publications

Title
Microscale Mechanical-Chemical Modeling of Granular Salt: Insights for Creep

Permalink
https://escholarship.org/uc/item/0tv87616

Journal
Journal of Geophysical Research: Solid Earth, 126(12)

ISSN
2169-9313

Authors
Hu, Mengsu
Steefel, Carl I
Rutqvist, Jonny

Publication Date
2021-12-01

DOI
10.1029/2021jb023112

Peer reviewed

Convergence of micro-geochemistry and micro-geomechanics towards understanding proppant shale rock interaction: a Caney shale case study in southern Oklahoma, USA

Allan Katende[a], Jonny Rutqvist[b], Margaret Benge[c], Abbas Seyedolali[d], Andrew Bunger[c,e], James O. Puckette[f], Andy Rhin[g], Mileva Radonjic[a,f,*]

[a]*School of Chemical Engineering, 420 Engineering North, Oklahoma State University: Stillwater, Oklahoma(OK) 74078, United States of America (USA).*
[b]*Energy Geosciences Division, Lawrence Berkeley National Laboratory, 1 Cyclotron Road, Berkeley, CA 94720, United States of America (USA).*
[c]*Department of Civil and Environmental Engineering, University of Pittsburgh, 710 Benedum Hall 3700 OHara Street Pittsburgh, PA 15261, United States of America (USA).*
[d]*Oklahoma Geological Survey, 100 East Boyd Street Sarkeys Energy Center Suite N131 Norman, OK 73019, United States of America (USA).*
[e]*Department of Chemical and Petroleum Engineering, University of Pittsburgh, 710 Benedum Hall 3700 OHara Street Pittsburgh, PA 15261, United States of America (USA).*
[f]*Boone Pickens School of Geology, Oklahoma State University: Stillwater, Oklahoma(OK) 74078, United States of America (USA).*
[g]*Continental Resources, Inc. 20 N Broadway Ave, Oklahoma City, OK 73102, United States of America (USA).*

Abstract

As a direct outcome of economic development coupled with an increase in population, global energy demand will continue to rise in the coming decades. Although renewable energy sources are increasingly investigated for optimal production, the immediate needs require focus on energy sources that are currently available and reliable, with a minimal environmental impact; the efficient exploration and production of unconventional hydrocarbon resources is bridging the energy needs and energy aspirations, during the current energy transition period. The main challenges are related to the accurate quantification of the critical rock properties that influence production, their heterogeneity and the multiscale driven physico-chemical nature of rock-fluid interactions. A key feature of shale reservoirs is their low permeability due to dominating nanoporosity of the clay-rich matrix. As a means of producing these reservoirs in a cost-effective manner, a prerequisite is creation of hydraulic fracture networks capable of the highest level of continued conductivity. Fracturing fluid chemical design, formation brine geochemical composition, and rock mineralogy all contribute to swelling-induced conductivity damage. The Caney Shale is an organic-rich, often calcareous mudrock. Many studies have examined the impact that clay has on different kinds of shale productivity but there is currently no data reported on the Caney Shale in relation to horizontal drilling; all reported data on the Caney Shale is on vertical wells which are shallow, compared to an emerging play that is at double the depth. In this work we develop geochemical-geomechanical integration of rock properties at micro-and nanoscales that can provide insights into the potential proppant embedment and its mitigation. The novel methodology amalgamates the following: computed X-ray tomography, scanning electron microscopy, energy dispersive spectroscopy, micro-indentation, and Raman spectroscopy techniques. Our results show that due to the multiscale heterogeneity in the Caney Shale, these geochemical and structural properties translate into a variation in mechanical properties that will impact interaction between the proppant and the host shale rock.

Keywords: Energy Transition, Caney Shale, Computed Tomography, Raman Spectroscopy, Energy Dispersive Spectroscopy, Indentation.

1. Introduction

Ever since the industrial revolutions of the eighteenth century, energy has been a vital element in determining how humans live. Todays high demand for energy has been driven by huge demographic and economic growth around the world (Kadoshin et al., 2000). Over the coming decades, a mix of energy will be used, consisting of dominantly fossil fuels (Middleton et al., 2017; Mohr et al., 2015) and supplemented by newer renewable sources (Duffy et al., 2020) such as geothermal and solar energy (Mwesigye and Yilmaz, 2021). As conventional reservoirs are depleting and are unable to match the energy demand, hydraulic fracturing of unconventional shale reservoirs is part of the ongoing search for new sources of energy (Gao et al., 2020; Huang et al., 2020; Middleton et al., 2017). Extensive research has been carried out in recent decades into the economic and environmental impact of gas shale production via hydraulic fracturing, driven by various controversies related to this technology, such as seismicity, pollution of underground

*Corresponding author
Email address:* mileva.radonjic@okstate.edu (Mileva Radonjic)

water and the need for transparency related to chemical design of hydraulic fracturing fluids (Meehan, 2016; Solarin and Bello, 2020; Yuan et al., 2015). Although shales have conventionally been used as sites for carbon dioxide storage (Busch et al., 2008), more recently attention has been paid to their value as hydrocarbon source rocks. Consequently, their potential as gas and oil reservoir rocks is now being exploited in several locations (Boyer et al., 2011).

Shale reservoirs are characterised by low levels of permeability and a very low matrix porosity (Clarkson et al., 2013; Davudov et al., 2020; Sun et al., 2020). Hydraulic fracturing is required if they are to be productive (Middleton et al., 2017). Improvements to horizontal drilling and hydraulic fracturing technology have allowed the production of large volumes of shale oil and gas; however, challenges remain in the area of quantifying the key geo-mechanical (Iferobia and Ahmad, 2020) properties of shale reservoirs, such as; strength, Youngs moduli, elasticity, plasticity, brittleness, ductility and fracture toughness. Elastic modulus, specifically, significantly impacts the hydraulic fracture aperture (Fjaer et al., 2008; Ma et al., 2020) during hydraulic fracturing, while hardness impacts on the proppant embedment (He et al., 2020; Mueller and Amro, 2015; Nakagawa and Borglin, 2019; Zhi and Elsworth, 2020), which in turn affects the fracture conductivity achieved.

Extensive studies have been conducted by multiple research teams (Antinao Fuentealba et al., 2020; Goral et al., 2020; Heng et al., 2020; Holt et al., 2020; Hou1 et al., 2019; Islam and Skalle, 2013; Kasyap and Senetakis, 2022; Minardi et al., 2021; Sone and Zoback, 2013a,b; Yin et al., 2019) over the last decade on the mechanical properties of shale that influence shale productivity, the majority have been at macro scale, as specimen size usually ranges from several millimeters to several centimeters. As an example, a considerable volume of rock material is required for researchers to carry out the uniaxial and triaxial compression test, which is the most commonly used in the determination of elastic modulus. Further limitations are that force-displacement curve analyses are subjective and macro tests cannot give a comprehensive understanding of the deformation mechanisms which underlie the stress-strain relation. Hence, micro (Du et al., 2020; He et al., 2020; Kasyap and Senetakis, 2022; Luo et al., 2020; Ma et al., 2020; Zong et al., 2006) tests are important to complement macro-scale testing due to their ability to study the micro-structural characteristics and thereafter deduce the mechanisms. These are understood to be tests in which the micro component is not specimen size, but the characteristic length of the objects under study. Changes in the micro-structure are simultaneously monitored, with specimens subjected to mechanical loading(s) under a microscope (Du et al., 2020; Hagen and Thaulow, 2016; Saif et al., 2017; Zhang et al., 2018) or

X-ray computed tomography device (Andrews et al., 2020; Crandall et al., 2017; Ma et al., 2020; Voltolini and Ajo-Franklin, 2020; Voltolini et al., 2021). Only this type of assessment therefore can enable researchers to make a truly accurate and rational comparison on the mechanistic factors that influence shale productivity.

1.1. Contribution and novelty of this study

The overarching goal of this study is;

1. There is no Correlative data set that combines Electron Microscopy, Raman Spectroscopy and Micro Indentation data on Caney Shale cores, as an effort to correlate geochemical composition to geomechanical response of the Caney shale.
2. Integration of 2D and 3D shale compositional heterogeneity, in terms of mineralogy, organic matter volume and distribution, on the micromechanical properties of the emerging Caney Shale play.
3. Understand the mechanisms of proppant embedment through application of correlative Raman spectroscopy with micro-indentation and scanning electron microscopy, and its potential translation into more effective completions technology for Caney shale wellbores.

Multiple scholars Anderson et al. (2020); Bai et al. (2013); Liu et al. (2017); Ma et al. (2020); Saif et al. (2017); Sharma and Sircar (2020) have attempted to delineate the impact that clay has on different kinds of shale productivity but there is currently no data reported on Caney shale in relation to horizontal drilling; all reported data is on vertical wells and in Caney formations that is shallow, compared to an emerging play that is at double the depth. However, there also remains a lack of understanding of the mechanisms involved.

The combination of the use of indentation techniques with Raman spectroscopy as a means of comprehending shale well production is an area that hasn't yet been assessed. The use of Raman spectroscopy is a non-invasive technique that can enable researchers look at a fractured wall in post API-RP61 test and no drying of a sample is required. We believe that this method can provide an understanding into trends and help connect to field performance that would enable more comprehensive completions and avoid fracture plugging and loss of production. By identifying insights into the composition matrix of the shale and the impact this has on its mechanical properties, we propose that it may be possible to adjust fracturing fluid composition such that it is precisely tailored to the mineral composition for the Caney Shale. This can potentially avoid proppant embedment and increase the production of stimulated shale volume.

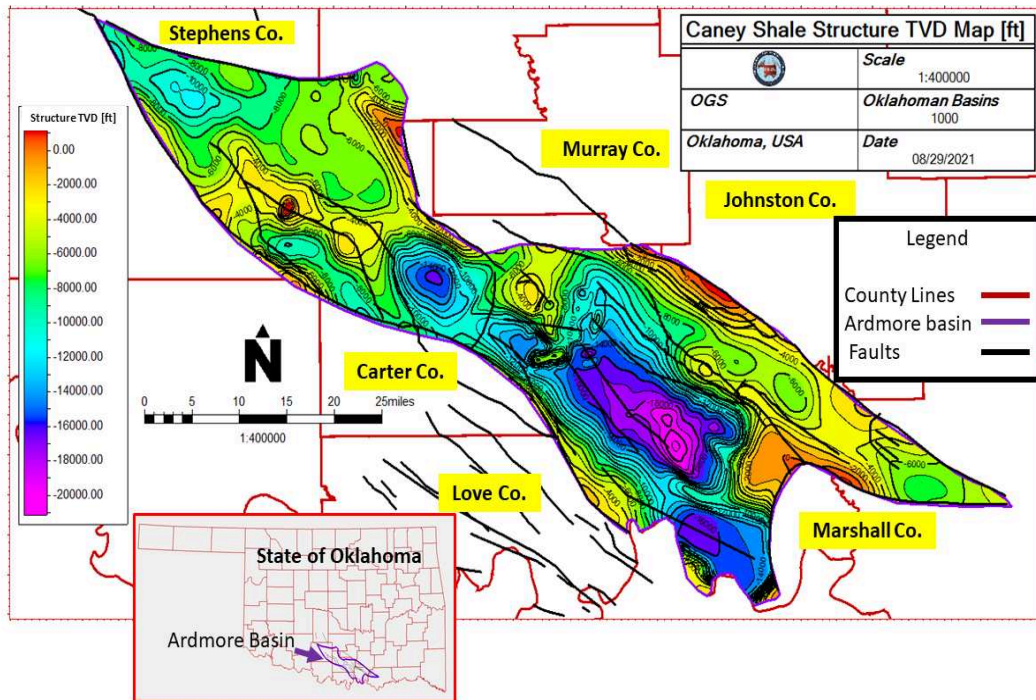## 2. Study Area and Geologic Setting of the Caney Formation

Figure 1: TVDSS structure map of the Caney Shale in the Ardmore and Marietta Basin, Oklahoma. The wells correspond to key locations and interpreted cores. County names highlighted in yellow.

The Caney shale shown in Figure 1, is located in the Arkoma basin, is stratigraphically comparable to the Barnett shale found in the Fort Worth Basin. In the aftermath of the significant success of the Barnett play, the formation has progressed to become a producer of gas and oil condensate (Andrews, 2007; Kamann, 2006; Maughan and Deming, 2006; Schad, 2004). The Caney shale is a large constituent composed of an organic-rich calcareous shale deposit that contains large concretions of carbonate (Radonjic et al., 2020). Over the past few years, it had become apparent that the way in which the Caney Shale is interpreted by geologists was based on the exposures in the Arbuckle Uplift (Andrews, 2007, 2012), while its name was derived from a location with little-known exposures.

The Caney Shale was initially annotated and named by Taff. (1901) Taff. (1901). According to Maughan and Deming (2006), in the 1920's, some degree of confusion in terms of the stratigraphic nomenclature of rocks found in basins within Oklahoma was introduced by petroleum geologists. The Pennsylvanian Caney term was applied to an area above the Caney. This was later formally renamed the Goddard Shale. Andrews (2003) used an alternative term, the False Caney, to describe a Goddard section.

According to Girty. (1909), the Caney shale is formed from a variety of exposures that are located throughout the Arbuckle within the central areas of the Chickasaw & Choctaw nations. The thickness of the shale does not exceed 1,000 feet, and it is formed of black and blue argillites that feature local sandy strata in the upper area. Although the majority of the Caney shale is black, the beds found in the upper area are lighter in color and potentially have a different fauna. Girty. (1909) also highlighted how some of the

Caney goniatites are also found in the Batesville sandstone and Fayetteville shale. This indicates that the Caney shale correlates with both these formations and the Moorefield.

Radonjic et al. (2020) microstructurally characterised the Caney Shale by evaluating an area of the Caney core spanning 200 ft that was extracted from a well drilled in 2007 located in southern Oklahoma. The outcomes of their analysis revealed that the Caney Shale is clay-rich dominated by illite. They also found matrix pores that ranged from nanometers to micrometres in scale.

Unlike the Barnett, Eagleford, Marcellus or even the Fayetteville, no one has developed a standard completion process for the Caney that will generate reliable production. Given that every shale play is different and what works for Barnett, Fayetteville, Eagleford is not guaranteed to work for Caney or any other shale play. This is because important differences exist in deposition, mineralogy, microstructure, and petrophysics characteristics.

3. Experimental Methods and Materials

3.1. Selecting samples from drilled Caney Cores

Table 1: Selected Formation intervals

Well Depth (ft)	Sample Name	Formation Description based on Well Log
X006	Sample A	Reservoir 1
X087	Sample B	Clay-rich formation
X139	Sample C	Reservoir 2
X171	Sample D	Clay-rich formation
X404	Sample E	Reservoir 3

The most critical decision, in selecting samples from retrieved drilled core for all laboratory investigations reported in this paper, was to focus on relevant rock properties with

regards to production. This was done by optically evaluating the entire core displayed for viewing and comparing it to the logs obtained during drilling, with industry and research partners present and involved in the selection decision. The common goal is that the drilling and completions of the future wellbores in Caney shale can benefit from detailed laboratory investigation and relevant modeling, which includes rock properties at various scales as well as the sample orientation with regards to the bedding of the rock and the impact on mechanical and chemical properties of the Caney shale during drilling, completions, and production.

The complete section of the Caney Shale was cored and recovered from a well drilled in January/February 2020 in the Ardmore Basin. This 650 feet of four-inch core was retrieved, cleaned, and petrophysically analyzed. A 1/3 slab was CT scanned at the NETL (the CT report will be published by NETL in 2021). The 2/3 core was viewed, and project team decision was made for locations from which plugs were retrieved The following samples varying in depth shown in Table 1 have been used in this study.

From the identified formation intervals shown in Table 1, core plugs were extracted at two different orientations that is; 45° & 90° as shown in Figure 2. Samples of 1" × 0.5" were cut using a diamond saw and then prepared for polishing. The core samples used in this study were fresh and acquired immediately after the core was recovered, cleaned and marked.

Core cleaning and sampling were conducted in a climate-controlled facility. Samples for mechanical properties tests were acquired first to ensure freshness and alleviate possible changes to the fabric and mineralogy resulting rock-atmospheric reactions. In addition, samples were taken from the cores interior to avoid rock that came in contact with coring and cleaning fluids.
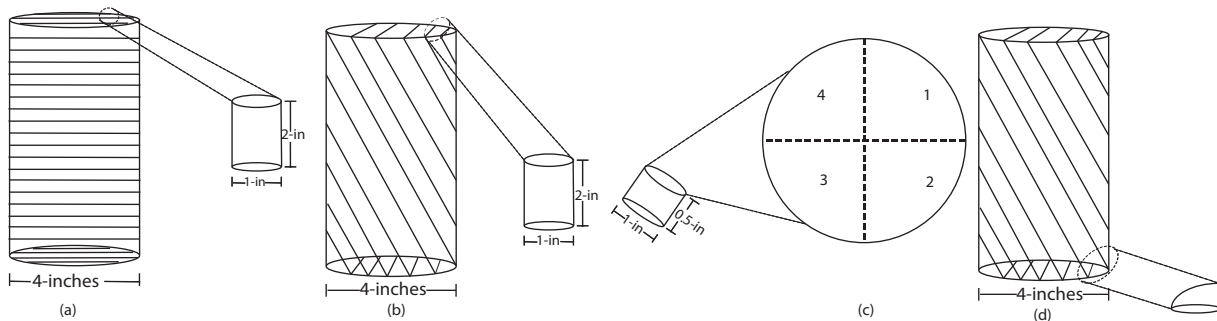

Figure 2: (a) Coring at 90 degrees to the bedding plane, (b). Coring at 45degrees to the bedding plane, (c) Sample surface on which SEM imaging and indentation shown in figure 3 was conducted after polishing(Section 3.2.2). The sample surface was divided into four quadrants to identify the effect of heterogeneity on all samples (d) End point of the cores that were trimmed and crushed into powder to represent bulk mineral composition.
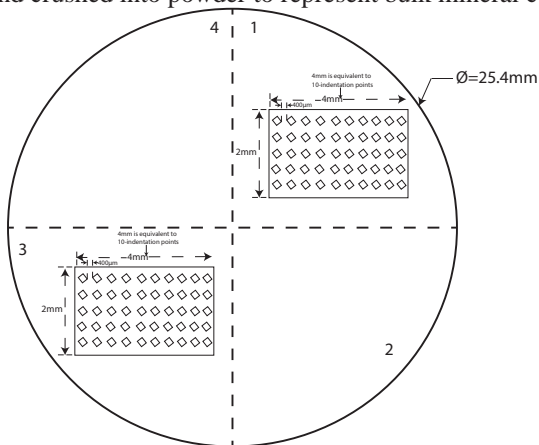

Figure 3: Illustration of how indentation was planned and executed on the Caney Shale polished samples.

3.2. Sample Preparation

Sample preparation was done in absence of water to prevent them from potential clay swelling.

3.2.1. Crushing of samples into powder

At each of the selected sample depth shown in Table 1, end point of the cores shown in Figure 2 were trimmed and crushed into powder to represent bulk mineral composition, twenty grams of crushed rock powder was used to identify the mineral composition.

3.2.2. Sample Polishing

After samples had been scanned(section 4.1) with an industrial CT scanner, they were then cut to 0.5-in in length as shown in Figure 2(c) and prepared for polishing. The Polisher shown in Figure A1 has been used for polishing all the samples. The purpose of polishing is to achieve better visibility on a scratch free surface under a microscope and during indentation. The various elements within the system were aligned to deliver the optimal outcomes and to make sure that the rotation axis sits upright to the platen and the fixture-mounting reference and the platen are parallel. The dimensions of the sample were used to cut a matching piece of sheet wax, which was subsequently affixed to the fixture for the purposes of the alignment. The sample was then positioned above the wax. The fixture, including wax, was heated on a hot plate at a temperature of 100^oc. After the wax had completely melted, the sample was cooled and subsequently stuck to the platen. The sample was then ground down until flat with the use of a 600-grit silicon carbide abrasive disk that was operated at 200 rpm and a sample load of 500g. This ensured that any deformation that remained after previous processing operations was fully removed, after which the sample was viewed under a microscope to verify the uniformity of the scratch

pattern. A fluid dispenser was employed to automatically dose the polishing lubricant and, thus, ensure the sample was prepared in a repeatable and consistent fashion. Purple lubricant which is perfect for water-sensitive samples was used during polishing and dispensed using button **1**. Deformation was removed via grinding using a 6μm diamond suspension on a gold-label polishing cloth with the purple lubricant dispensed using button **2** at 150rpm and a sample load of 500g and 1μm diamond suspension on a white-label polishing cloth in combination with the purple lubricant dispensed using button **3** at 150 rpm. The sample then underwent a final processing step that involved the use of a 0.05μm water-free colloidal silica suspension dispensed using button **4** at 150rpm and a sample load of 500g on a Chem-pol polishing cloth. All samples were polished over a sustained duration to make sure any deformations were removed and, as such, the specimens were suitable for electron back-scattered diffraction analysis. After a sample had been sufficiently prepared, it was removed from the parallel polishing fixture, inspected under a microscope and the process was repeated for each sample.

3.3. Experimental Techniques
3.3.1. Computed Tomography Scan of the Samples

1-in×2-in core plugs were drilled from 4-in cores at different orientations as shown in Figure 2. These were then scanned using an industrial medical CT scanner from the National Energy Technology Laboratory(NETL). Core plugs were scanned using a sub-millimeter core-scale resolution of 91μm× 91μm× 100μm with a voltage of 135kV and a current of 200mA.

3.3.2. X-ray Diffraction(XRD) analysis

At each of the selected sample depth shown in Table 1, twenty grams of crushed rock powder was used to identify the mineral composition wiith a Bruker D8 Advanced X-ray Diffraction(XRD) instrument in the Venture I facility at Oklahoma State University Laboratory that is coupled with a Lynxeye detector.

3.3.3. Scanning Electron Microscopy(SEM)

SEM imaging was carried out using a FEI Quanta 600 field-emission gun Environmental Scanning Electron Microscope illustrated in Figure A2, in both secondary electron mode and in the backscattered electron mode. Images, maps and spectra were obtained at 20KeV, and various magnifications, from a larger field of view to a higher magnification that revealed characteristics of interfaces and surface properties of various phases. SEM images are necessary to describe and classify the pore types in the Caney Shale. In addition, energy dispersive spectroscopy was used to obtain chemical elemental maps, to identify components not detected by XRD and assess the surface chemistry of the Caney Shale and how these elemental components might impact its response to hydraulic fracturing.

Samples of interest were scanned in back-scatter mode because it provides a good illustration of the different components in shale particularly because polished samples are flat creating a least possible topography and contrast which is the basis for secondary electron image interpretation. Once all the quadrants (shown in Figure 2c) for all the samples of interest were scanned, the system was vented and samples were taken out and the chamber was closed.

3.3.4. Raman Spectroscopy

Over the last ten years, Raman spectroscopy has evolved (Chen et al., 2019; Truong-Lam et al., 2020) to become an extremely effective approach in analytical science because of its molecular sensitivity and ease of implementation. Furthermore, unlike Infrared radiation spectroscopy, the presence of liquids (Bodnar and Frezzotti, 2020) does not hinder the applicability of Raman spectroscopy. Confocality (Turrell and Corset, 1996) plays a fundamental role in suppressing undesirable fluorescence background and any backgrounds from substrates, which can potentially serve to mask the signal of a thin coating layer. The use of Raman spectroscopy is vital in alleviating the limitations of wavelength dispersive X-ray fluorescence(WDXRF) by identifgying a precise composition of mineralogy on sample at scales less than 1μm without any sample preparation (Stemmermann et al., 2020) .

The procedure for Raman (Figure A3) testing involved loading the sample onto the sample stage and a video mode was enabled to ensure that the sample surface is seen. An appropriate lens was chosen and the sample was placed in focus of the microscope using a joy-stick control pad. Once the sample was in focus, a video image was acquired and the Raman microscope was then turned to Raman mode. Using the control software, and a combination of power and integrated time was chosen. To generate Raman spectra the following parameters were used: 20X and 50X objective lenses, an excitation wavelength from the 532nm laser distributed by a 600 g/mm BLZ=500nm grating, a laser power between 0.5–5 mW and an integration time of 1s. Raman spectra were then acquired using points and an area scan was done. Ten accumulations were measured on each acquisition on all the samples so as to minimize noise on spectra obtained. Once the Raman scan was done, the set-up was changed to video mode and the sample was unloaded. The procedure was repeated for all the subsequent samples.

3.3.5. Laser Surface Profilometry

The laser surface profilometer linked to the Raman microscope was used for quantifying the indentation depths on each of the indented samples. Samples were placed under a Raman microscope shown in Figure A3. To obtain a surface profilometry map, the following parameters were used: 20X and 50X objective lenses, an excitation wavelength from the 532nm laser distributed by a 600 g/mm BLZ=500nm grating, a laser power between 0.55 mW.

3.4. Micro/Nano Indenter

The indenter illustrated in Figure A4 was used in determining the mechanical properties of the Caney Shale. The procedure for indentation on shale samples involved firstly ensuring that the anti-vibration table is pressurised to about 20psi to prevent any imperfections during the test. This was subsequently followed by calibrating the vickers diamond indenter tip using a steel block provided for calibration to ensure that the elastic modulus and hardness obtained during indentation are comparable to the ideal values of steel. Once this was achieved, a test sample was loaded as shown in Figure A4. The indenter tip was manually lowered until it was visibly close to the sample surface. The contact surface

for the sample was identified by doing an contact procedure with an indenter tip load of 20N and a speed of 500N/m. When the indenter tip made contact with the sample, the indenter tip was raised to 0.5μ above the sample surface and a the indenter tip was moved to a new location. The next step involved calibrating the depth sensor. As soon as the depth sensor was calibrated, the indenter tip was moved to the test location. In all out tests, we use a test load of 5N and integrate the effect of creep by holding the indenter tip for 30s when it reached the maximum load and then unloading of the tip preceded.
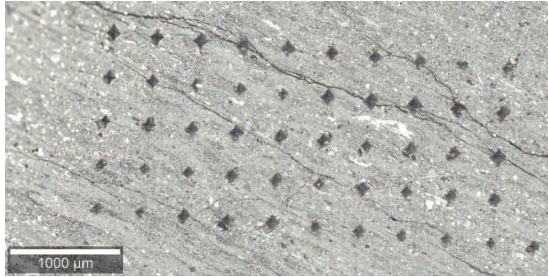
Figure 4: Illustration of the final surface after indentation. This was obtained using a Raman Surface Profilometry described in section 3.3.4 conducted in Quadrant 1 of Sample B @ 90° to bedding .

To investigate heterogeneity, fifty indentation tests were carried out using a 10×5 indentation pattern and a spacing of 400μm between each indent as shown in Figure 3& Figure 4 . Indentation was carried out in quadrants 1 and 3 after conducting an SEM(see section 3.3.3) analysis that indicated that quadrants 1&2 as well as quadrants 3&4 have no micro-structural difference but there was a significant difference between quadrants 1&3 for all the samples.

Figure 5 shows the load versus displacement curve during indentation and a schematic of the indentation impress after load removal taken with the 5X objective lens linked to the indenter described in Figure A4.

The mechanical properties were computed using the Oliver and Pharr (1992) empirical relationships described below:

1. Hardness was computed from equation 1;

$$H = \frac{F_{max}}{A_c} \quad (1)$$

- where F_{max} is the maximum load applied
- A_c is the projected area of the vickers diamond tip and is computed from equation 2;

$$A_c = 4 \cdot h_c^2 \cdot tan^2\theta \equiv 4 \cdot h_c^2 \cdot tan^2 68 \equiv 24.5 \cdot h_c^2 \quad (2)$$

- h_c represented in Figure 5 is the vertical distance of contact from the tip and is computed from equation 3;

$$h_c = h_{max} - h_f \equiv h_{max} - \left[\frac{3F_{max}}{4S}\right] \quad (3)$$

- S is computed from the slope of Figure 5 as;

$$S = \left[\frac{dF}{dh}\right]_{unloading} \quad (4)$$

2. Young's modulus(E) was computed from equation 5;

$$E = \frac{\left(1 - \upsilon^2\right)E_r \cdot E_i}{E_i - \left[\left(1 - \upsilon_i^2\right)E_r\right]} \quad (5)$$

- E_i is the indenter modulus.
- υ_i is the indenter Poisson's ratio.
- υ is the sample Poisson's ratio.
- E_r is the reduced modulus given by $E_r = \frac{\sqrt{\pi} \cdot S}{2 \cdot \sqrt{A_c}}$.
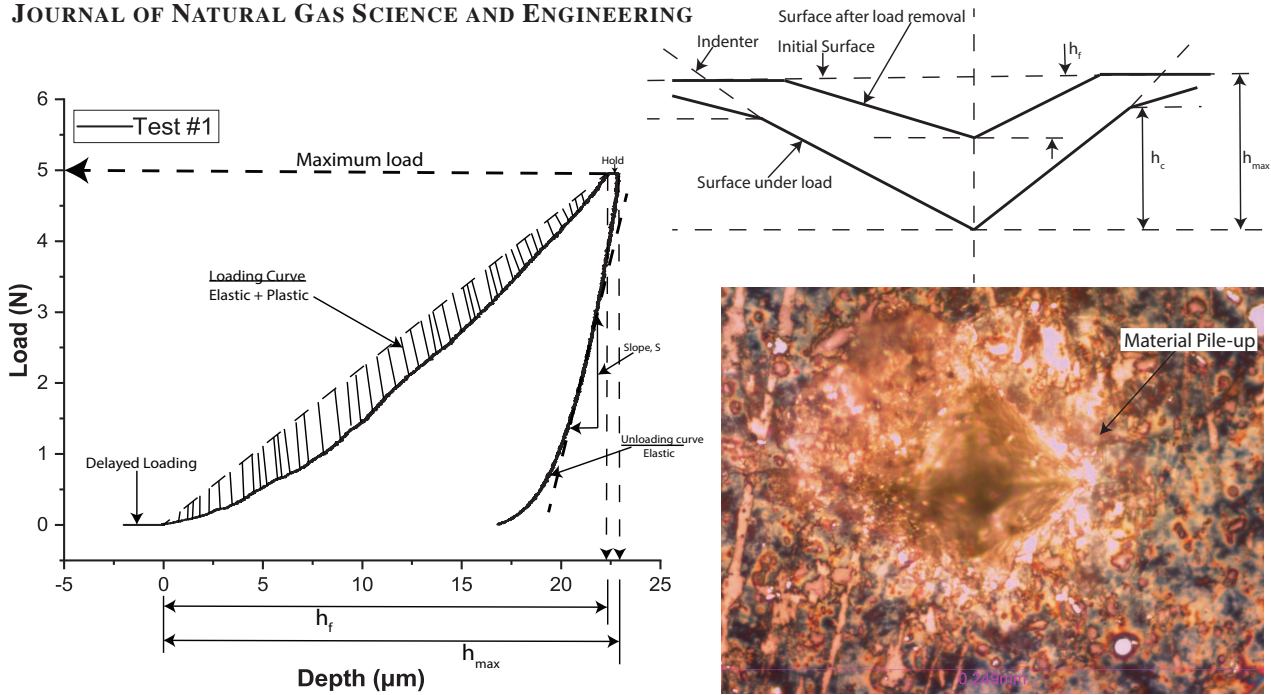
Illustration of a load displacement curve after load removal.

Illustration of an Indentation Impress after load removal.

Figure 5: Load versus displacement curve during indentation and illustration of the indentation impress after load removal.

4. Results

The results from this study were organized to demonstrate how heterogeneity of shale rocks resulting from mineral composition, carbon content, structure and texture, and pore structure is relevant to geochemical, geomechanical and mineralogical properties that may impact proppant embedment. The description of the results begins by presenting CT-scans of 1 x 2 inch core plugs, which show the importance of sample orientation to the rocks, depositional bedding as well as providing an insight on mineralogical heterogeneity and presence of fractures. The CT scans showed properties of the rock, but compositional XRD results that is focused on bulk analysis showed clay-carbonate-quartz versus metallic type of minerals present. The results are all quantitative except for differentiating various types of clays which was not completely achieved with the available techniques. From the bulk analysis obtained from CT-scans and XRD, we then narrow down and look at the Raman spectroscopy analysis that can capture organic content, which we were not able to identify chemically under the SEM/EDS. This is followed by the microstructure of the rock in a scanning electron microscope (SEM) and the corresponding microchemistry as captured using Energy Dispersive Spectroscopy (EDS). We finish the results section with the micro-mechanical properties that were obtained using 2D mapping of polished surfaces with a micro-indenter and the results are presented in section 4.4. The post indentation analysis with the laser surface profilometry was critical to understand how potential proppant embedment would be related to the mineralogical 2D maps obtained using EDS maps and the indenter marks are presented in context with the elemental maps in section 4.5.

4.1. Computed Tomography Scans of the Samples.

Figure 6 shows two-dimensional isolated planes through the vertical center of the samples as scanned with the medical computed tomography scanner at the NETL. The 1X2in cylindrical core plugs after coring show a significant variation in structure and fabric of the shales. The CT scans were conducted using a voltage of 135kV and a current of 200mA with a Toshiba Acquilon RKL medical CT scanner. In the greyscale images shown in Figure 6 the bright zones are high density minerals and the dark zones are voids and fractures. Overall, Sample A cored at 90° to the bedding showed distinct features having a fracture filled by secondary mineralization because of fibrous mineral growth. Samples B, C, and E cored at 90° to the bedding exhibited natural fractures whereas sample E cored at 45° to the bedding exhibited pyrite on the CT scans because it is an electrical highly conductive mineral. Cross bedding and natural fractures are observed in samples cored at 45° to the bedding.
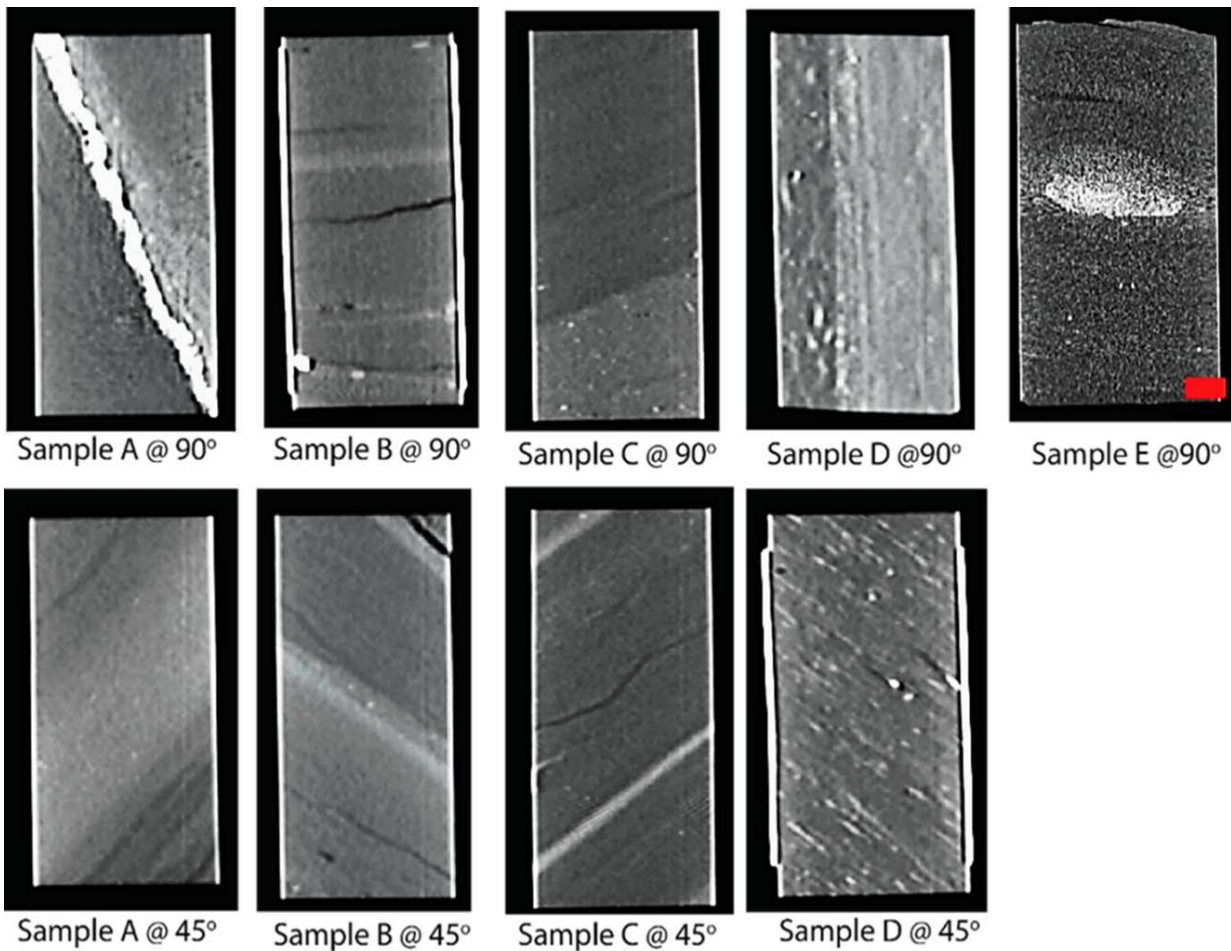
Figure 6: 2D isolated planes through the vertical center of the medical CT scans of the 1×2-inch core plugs described in section 3.1. CT scans were conducted using an industrial CT medical scanner from the National Energy Technology Laboratory(NETL).

4.2. Rock fabric composition, Mineralogy and Total Organic Content

Rock fabric and composition are major factors controlling mechanical properties of shales. Diagenetic processes, especially cementing enhance brittleness and make the rock more amenable to natural fracturing and less-prone to embedment. Cemented fractures tend to reopen during stimulation and the layer of cement adhering to the fracture wall armors it against embedment. Silica and calcite cement are essential to the success of the Woodford Shale and Barnett Shale plays, respectively, and are important factors in successful shale plays (Allix et al., 2010). Organic content is critical to shale plays as it is not only the source of oil and gas contained in source/reservoir mudrocks, but organic content provides storage for oil and gas within in intraorganic pores formed by the loss of volume during the conversion of solid kerogen/organic matter to liquid or gaseous hydrocarbons (Loucks et al., 2012).

4.2.1. Composition of the Rock fabric as revealed by XRD

Powder X-ray diffraction shows that mineralogy varies across the five (5) samples. Quartz is the most common rock constituent and ranges from a low of approximately 39% in sample E to 64% in sample A. Clay minerals critical to ductile behavior such as illite and mixed layer illite-smectite range from a combined low of about 11% in sample A and B to 29% in sample D. Carbonate minerals calcite, dolomite and ankerite combined reach a high of 26% in sample E are lowest in sample D with 7%.
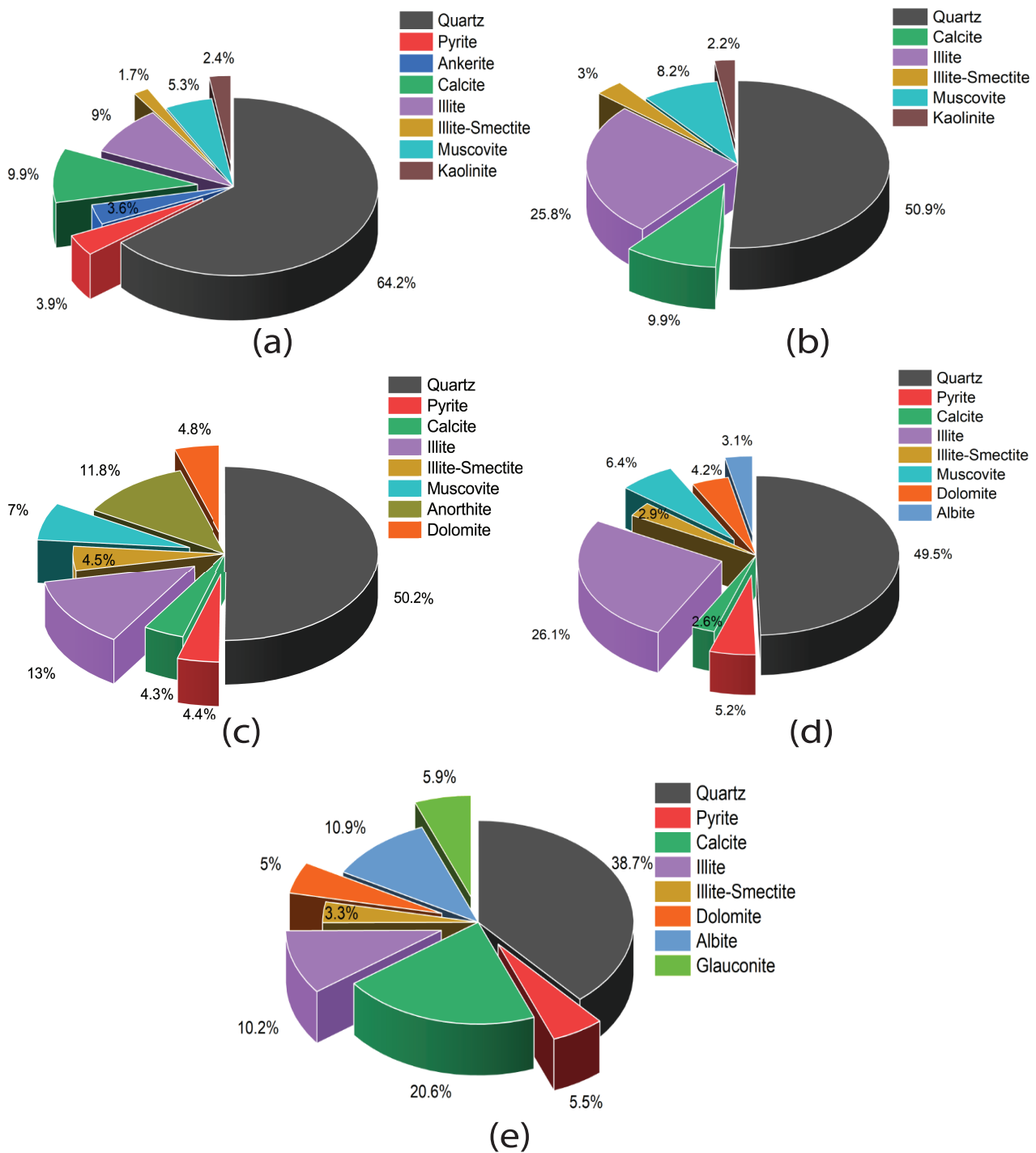
Figure 7: Mineral composition of the Caney Shale samples described in section 3.1 as revealed through XRD analysis. (a)Sample A, (b)Sample B, (c)Sample C, (d)Sample D, (e)Sample E.

The five pie charts shown in figure 7 compare the composition of the rock fabric for the five samples described in Table 1 of section 3 as revealed through XRD analysis. Overall, it can be seen that the percentage of clay mineral constituents vary with the depth of each sample. The bulk of quartz content in the samples whose composition was 64.2% came from Sample A followed by sample C, Sample B, Sample D and leastly sample E. In contrast to the illite content, the largest proportion of illite content which was 26.1% came from Sample B followed by sample C, Sample E, Sample A and lastly Sample B. Moving on to other constituents such as calcite, dolomite, Ankerite, Muscovite and Kaolinite varying proportions are seen in all the Samples. In detail, the largest percentage of calcite which is 20.6% came from Sample E followed by Samples A&B, Sample C, and Sample D.

Radonjic et al. (2020) noted that the higher the clay mineral content, the more ductile the sample is whereas a lower clay mineral content indicates brittleness.

530 *4.2.2. Raman Spectroscopy Analysis and Surface Chemistry*
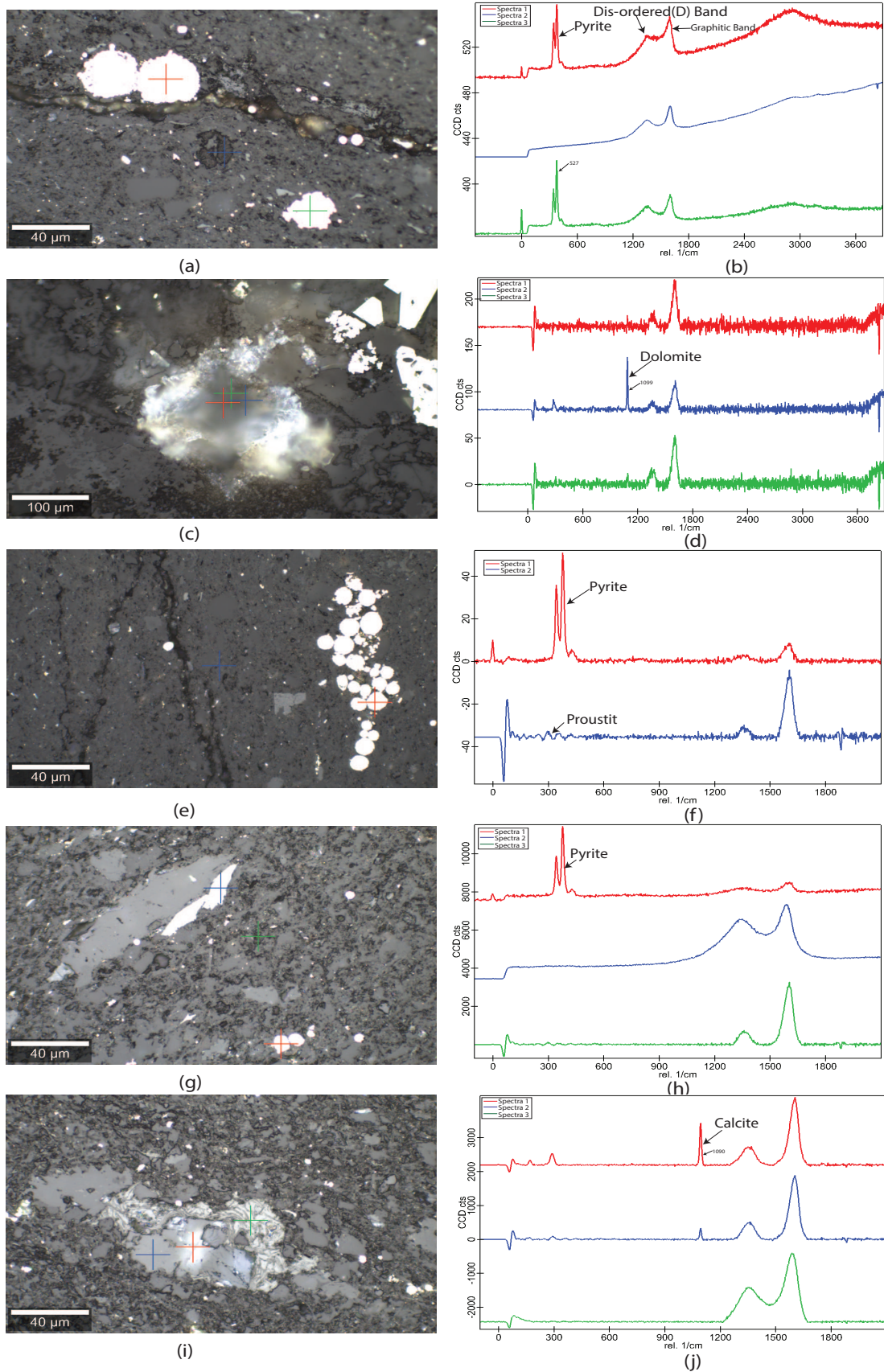
Figure 8: Raman identification of minerals from the Caney Shale samples described in section 3.1 before indentation (a)&(b)Sample A, (c)&(d)Sample B, (e)&(f)Sample C, (g)&(h)Sample D, (i)&(j)Sample E.
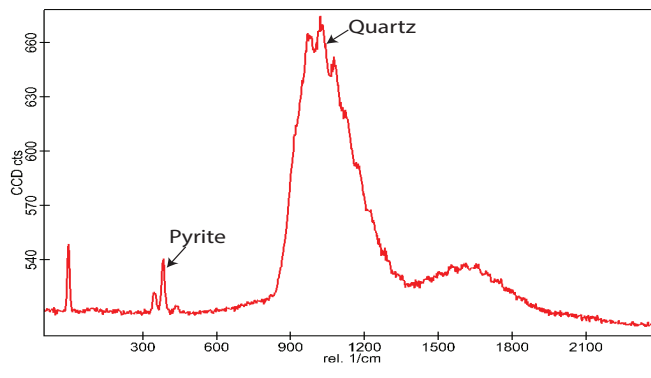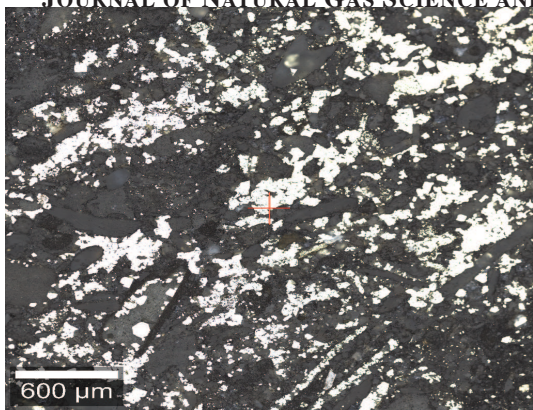
Figure 9: Raman identification of minerals from Sample A of the Caney Shale samples described in section 3.1 before indentation.

Raman spectra can be used to determine the molecular vibrational frequency and the surface chemical composition of a variety of materials (Bodnar and Frezzotti, 2020; Chen et al., 2019; Lubwama et al., 2013; Sarycheva and Gogotsi, 2020; Stemmermann et al., 2020; Truong-Lam et al., 2020) and quantify their phases including a myriad of minerals that includes organic material in gases and rocks. The surface chemistry of shale is of critical importance because it determines the interactions of fluids and proppants with the rock. As such, Raman spectroscopy is useful because it could facilitate the identification of very small grains that are difficult to identify through the use of conventional optical microscopy which is limited to a bulk configuration of the intermixed phases. Raman spectroscopy is an objective, reproducible and non-destructive method for examining particles, cuttings, cores, plugs or thin sections of materials and the presence of liquids (Bodnar and Frezzotti, 2020) doesn't hinder its applicability. The Raman shift indicates the arrangement of molecules and molecular bonds, allowing a distinction to be made between minerals that have the same composition but different underlying structures. The atoms are arranged differently in those crystals; as such, the spectra varies.

Figures 8(a)&(b) show the identification of pyrite(FeS_2) nodules on analysis of sample A. Figure 8(c)&(d) depict dolomite$\{CaMg(CO_3)_2\}$ spectra on analysis of Sample B.

Figures 8(e)&(f) show the identification of pyrite(FeS_2) nodules on analysis of sample C. Figures 8(g)&(h) show the identification of pyrite(FeS_2) nodules on analysis of sample D. Figures 8(i)&(j) show the identification of calcite($CaCO_3$) crystals on analysis of sample E. A further analysis of sample A depicted pyrite(FeS_2) and quartz(SiO_2) crystals as shown in Figures 9(k)&(l).

It can be seen in Figure 8 in all spectra acquired from different samples that there exists a broadband centered at roughly $1360 cm^{-1}$ termed as the D-band and referred to as the disordered band while a narrower band centered at approximately $1604 cm^{-1}$ termed as the G-band which stands for graphitic band. This is becuase during categenesis and metagenesis (Tissot and Welte, 1978), the chemical structure of organic matter is fundamentally changed. The thermal maturation of kerogen is called graphitization which generally thought to take place later in the metagenetic process and occurs due to the loss of hydrogen-rich aliphatic carbon groups, resulting in hydrogen-poor residual kerogen dominated by aromatic carbon structures. Organic matter that is dominantly kerogen under metamorphic conditions decomposes leading to the creation of pure carbon in the form of graphite. These observations are consistent with findings from other researchers (Foucher et al., 2017; Henry et al., 2018; Tuschel, 2013; Yakaboylu et al., 2020).
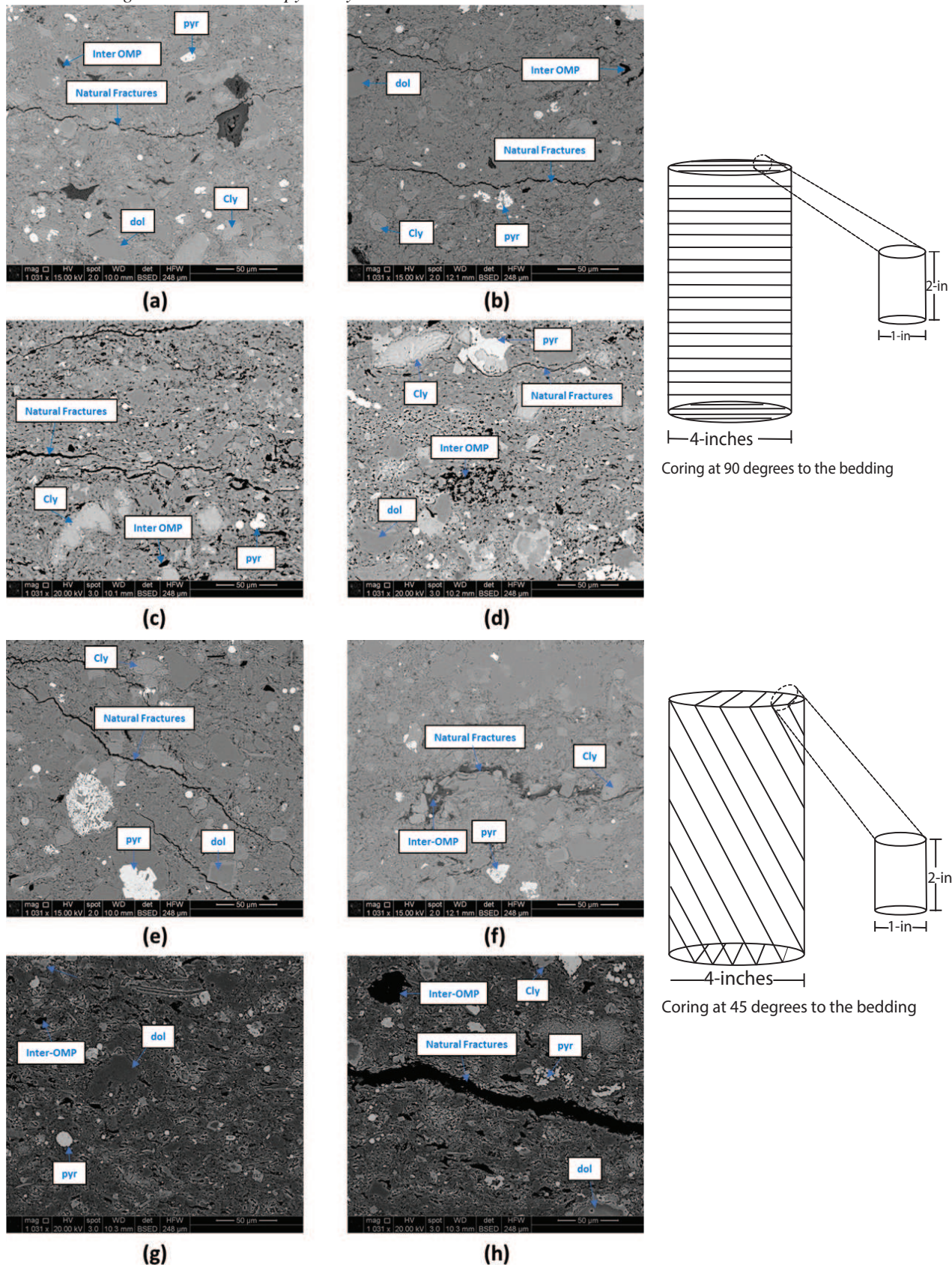
4.3. Scanning Electron Microscopy and Energy Dispersive Spectroscopy Analysis

583 *4.3.1. Scanning Electron Microscopy Analysis*

Figure 10: (a)Sample A @45°, (b) Sample A @90°, (c) Sample B @45° (d) Sample B @90° from quadrant 1; (e) Sample A @45°, (f) Sample A @90°, (g) Sample B @45° (h) Sample B @90° from quadrant 3 : to bedding orientation SEM Backscatter Electron Diffraction (BSED) micrographs at 20kV and 1030X of sections within the Caney Shale. In the backscatter mode, heavier elements appear brighter and thus pyrite is seen to be dominant. All images were acquired before indentation on polished an uncoated samples and they indicate existence of dolomite, Quartz, pyrite, and natural fractures.
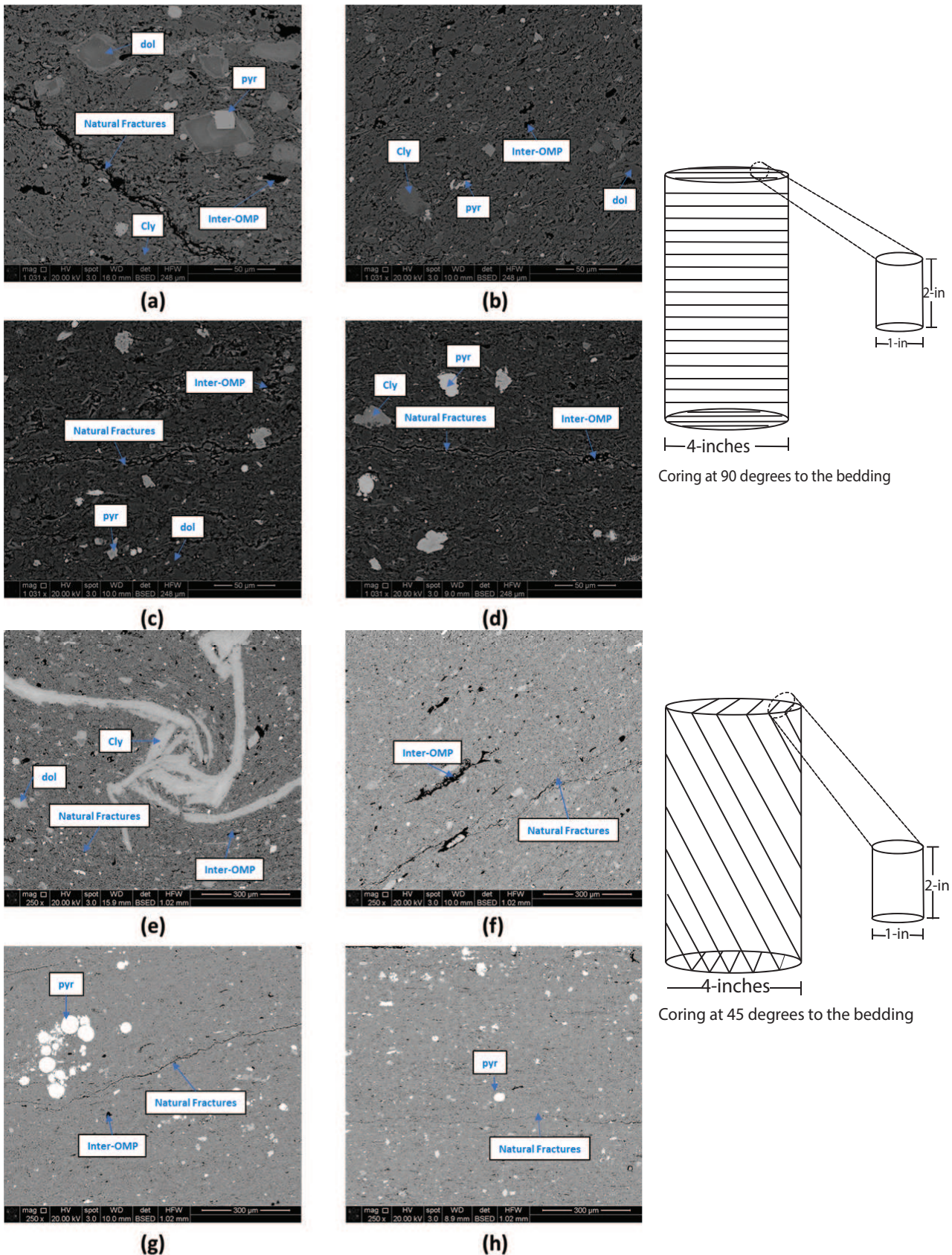
Figure 11: (a) Sample C @45°, (b) Sample C @90°, (c) Sample D @45° (d) Sample C @90° from quadrant 1; (e) Sample C @45°, (f) Sample C @90°, (g) Sample D @45° (h) Sample D @90° from quadrant 3 : to bedding orientation SEM Backscatter Electron Diffraction (BSED) micrographs at 20kV and 1030X of sections within the Caney Shale. In the backscatter mode, heavier elements appear brighter and thus pyrite is seen to be dominant.All images were acquired before indentation on polished an uncoated samples and they indicate existence of dolomite, Quartz, pyrite, and natural fractures..
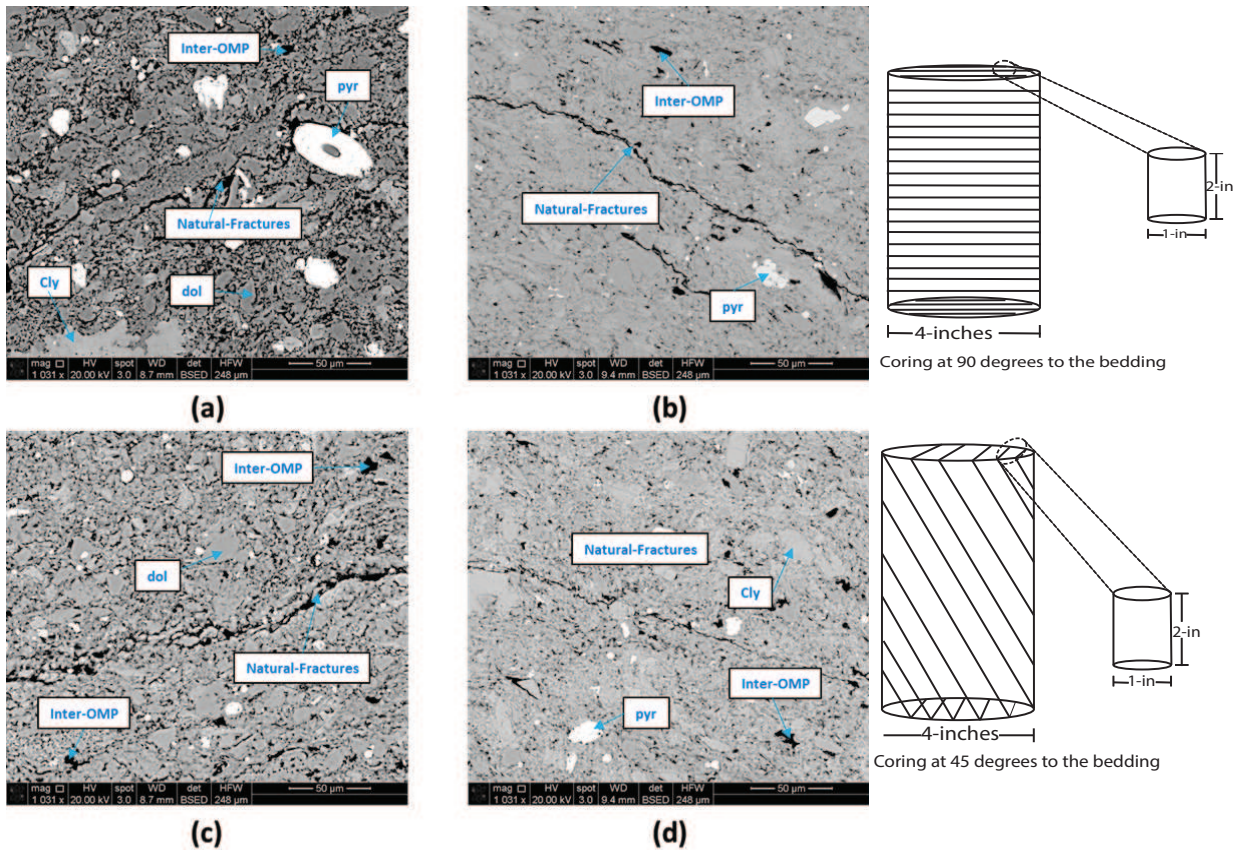
Figure 12: (a) Sample E @45°, (b) Sample E @90° from quadrant 1; (c) Sample E @45°, (d) Sample E @90° from quadrant 3 : to bedding orientation SEM Backscatter Electron Diffraction (BSED) micrographs at 20kV and 1030X of sections within the Caney Shale. In the backscatter mode, heavier elements appear brighter and thus pyrite is seen to be dominant.All images were acquired before indentation on polished an uncoated samples and they indicate existence of dolomite, Quartz, pyrite, and natural fractures.

Scanning electron microscope(SEM) was utilized to study the micro-structure and morphology of the samples described in section 3.1. The results illustrated in Figures 10, 11, 12 indicate heterogeneity and that the samples consist of mainly: pyrite, dolomite,micro-porosity, organic matter, natural fractures and clays. In all the quadrants shown in Figure 2(c), SEM images were acquired using the backscatter mode as opposed to secondary electron mode because it provides a good illustration of the different components in shale particularly because polished samples are flat creating the least possible topography and contrast which is the basis for secondary electron image interpretation. From the backscatter images, compositional variation in dark and bright areas are observed. Organic matter appeared as dark masses whereas pyrite appeared in a spheroidal cluster and displays as a bright element when imaged in a backscatter mode under the SEM. The micro-porosity seen in Figures 10, 11, 12 is associated with organic matter. This is attributed to the thermal maturation of organic matter during burial diagenesis and catagenesis resulting in formation of a pore network of bitumen and mobilized hydrocarbons within the organic material. This process then creates channels of pores in the organic matter.

Furthermore, a variation in micro-structure and mineralogy is observed from Figures 10, 11, 12 as the orientation changes indicating that micro-structural and mineralogical changes are dependent on bedding orientation.

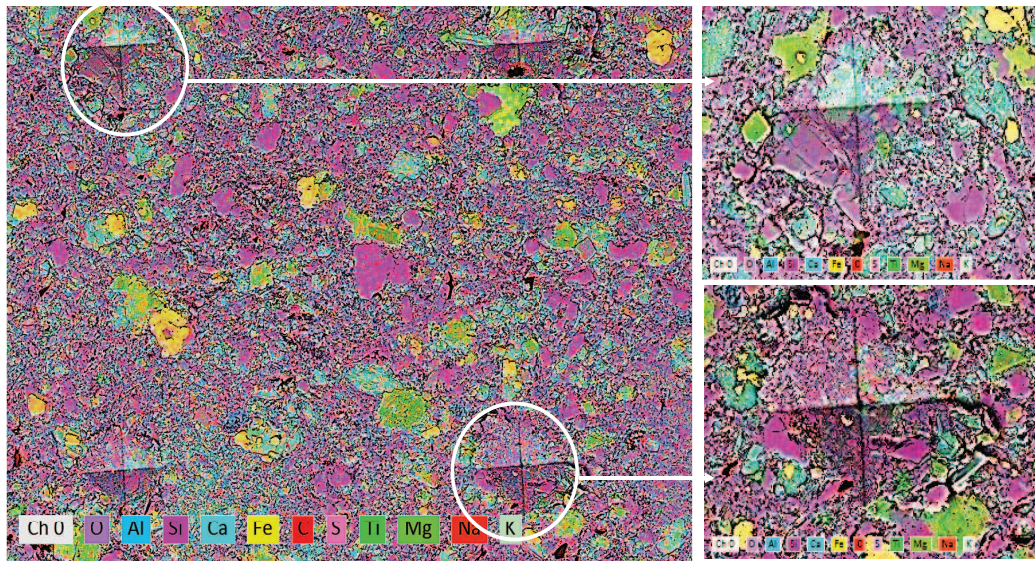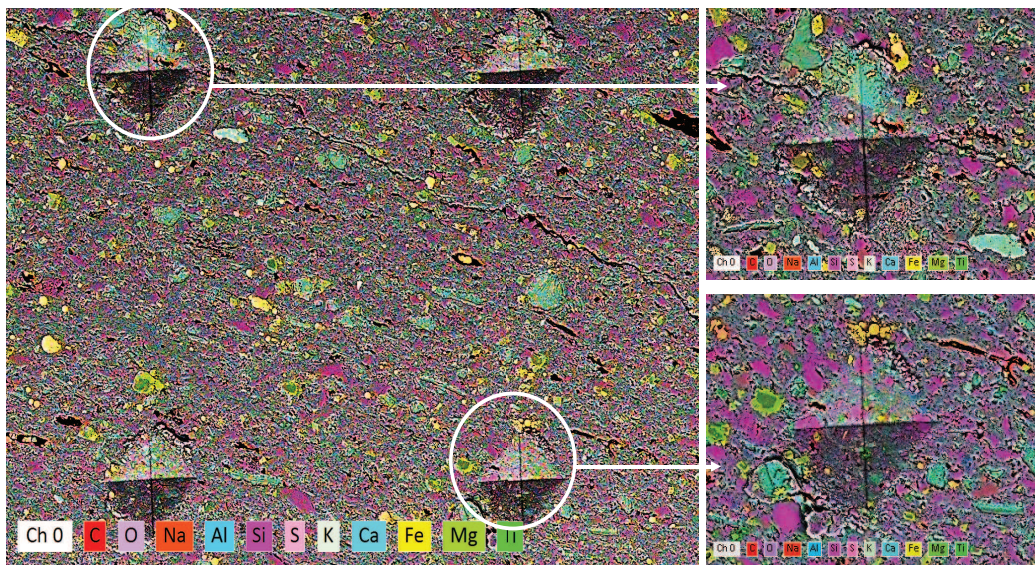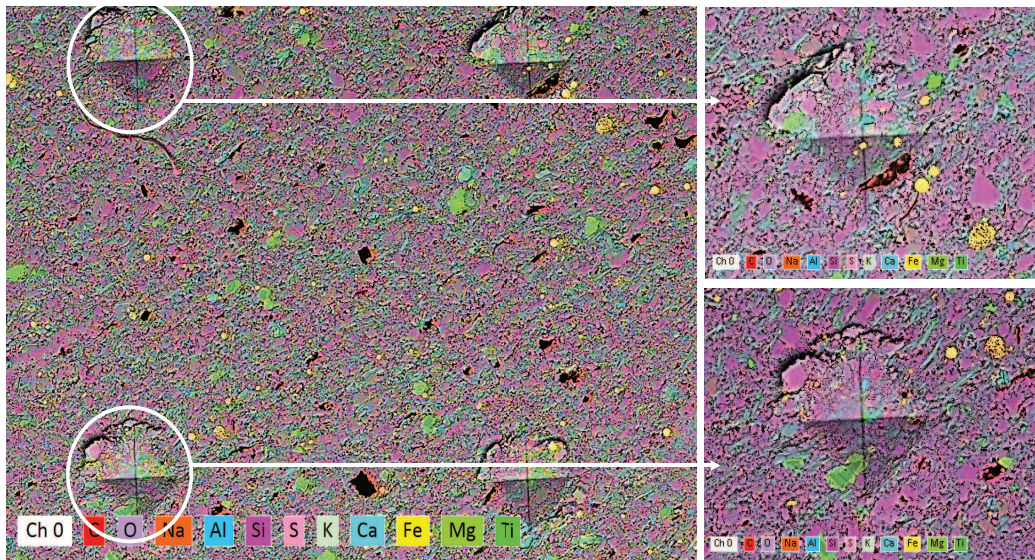*4.3.2. Energy Dispersive Spectroscopy Analysis*

Figure 13: Surface Chemistry of the Sample A as revealed by the Energy Dispersive Spectroscopy. SEM micrographs were acquired using a Backscatter Electron Diffraction (BSED) mode at 20kV in areas where indentation was done. Yellow is most likely FeS$_2$ or Pyrite. Pale blue is Calcite, magenta is quartz, green-blue is dolomite, and majority of fine-grained matrix are different types of clays
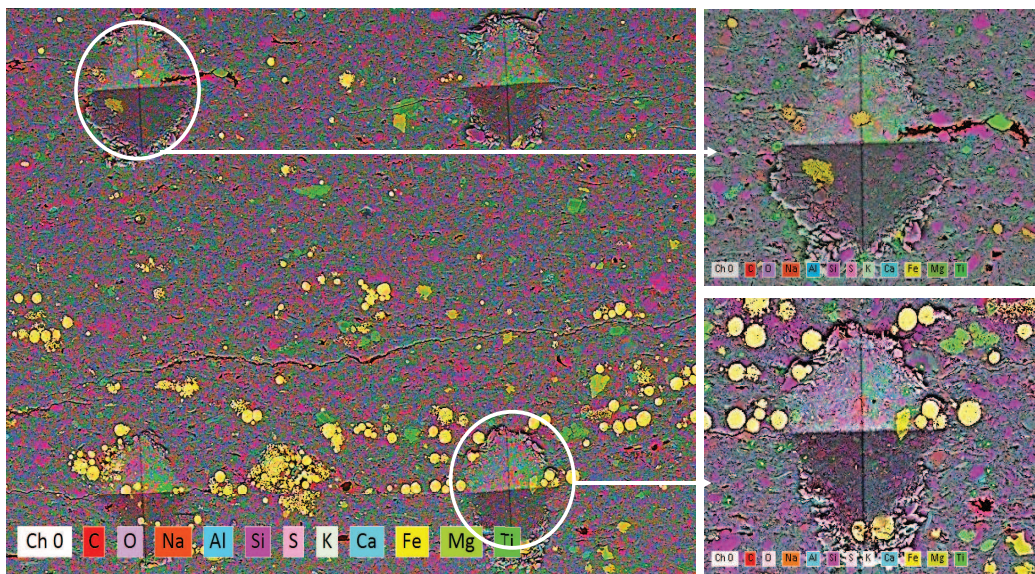

Figure 14: Surface Chemistry of the Sample B as revealed by the Energy Dispersive Spectroscopy. SEM micrographs were acquired using a Backscatter Electron Diffraction (BSED) mode at 20kV in areas where indentation was done. Yellow is most likely FeS$_2$ or Pyrite. Pale blue is Calcite, magenta is quartz, green-blue is dolomite, and majority of fine-grained matrix are different types of clays
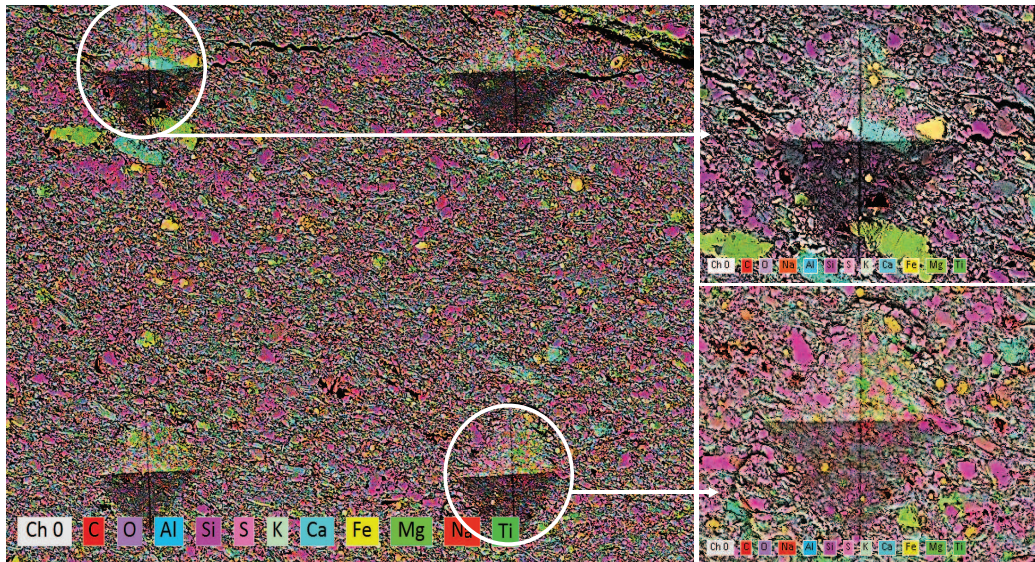
Figure 15: Surface Chemistry of the Sample C as revealed by the Energy Dispersive Spectroscopy. SEM micrographs were acquired using a Backscatter Electron Diffraction (BSED) mode at 20kV in areas where indentation was done. Yellow is most likely FeS_2 or Pyrite. Pale blue is Calcite, magenta is quartz, green-blue is dolomite, and majority of fine-grained matrix are different types of clays

Figure 16: Surface Chemistry of the Sample C as revealed by the Energy Dispersive Spectroscopy. SEM micrographs were acquired using a Backscatter Electron Diffraction (BSED) mode at 20kV in areas where indentation was done. Yellow is most likely FeS_2 or Pyrite. Pale blue is Calcite, magenta is quartz, green-blue is dolomite, and majority of fine-grained matrix are different types of clays

Figure 17: Surface Chemistry of the Sample C as revealed by the Energy Dispersive Spectroscopy. SEM micrographs were acquired using a Backscatter Electron Diffraction (BSED) mode at 20kV in areas where indentation was done. Yellow is most likely FeS_2 or Pyrite. Pale blue is Calcite, magenta is quartz, green-blue is dolomite, and majority of fine-grained matrix are different types of clays

The surface chemistry of shale is of critical importance because it determines the interactions of fluids and proppants with the rock. As such, EDS analysis was conducted because it could facilitate the identification of mineral phase variation along the grains. Samples were coated with carbon and loaded into the SEM chamber(Figure A2), SEM micrographs were taken in areas where indentation had been conducted and an elemental composition analysis was done using EDS. EDS analysis of Samples A,B,C,D&E are presented. Figures 13, 14, 15, 16, 17 show the SEM micrograph and elemental compositions of of Samples A,B,C,D&E. All Figures show heterogeneity in the spatial distribution of the minerals but the elemental constituents are common in all; pyrite, calcite, dolomite and quartz is seen in all the samples. However, Sample D shown in Figure 16 shows a higher concentration of framboidal pyrite on the surface. The findings from EDS analysis agree with the surface chemistry findings from the Raman Spectroscopy presented in Figure 8, and Figure 9.
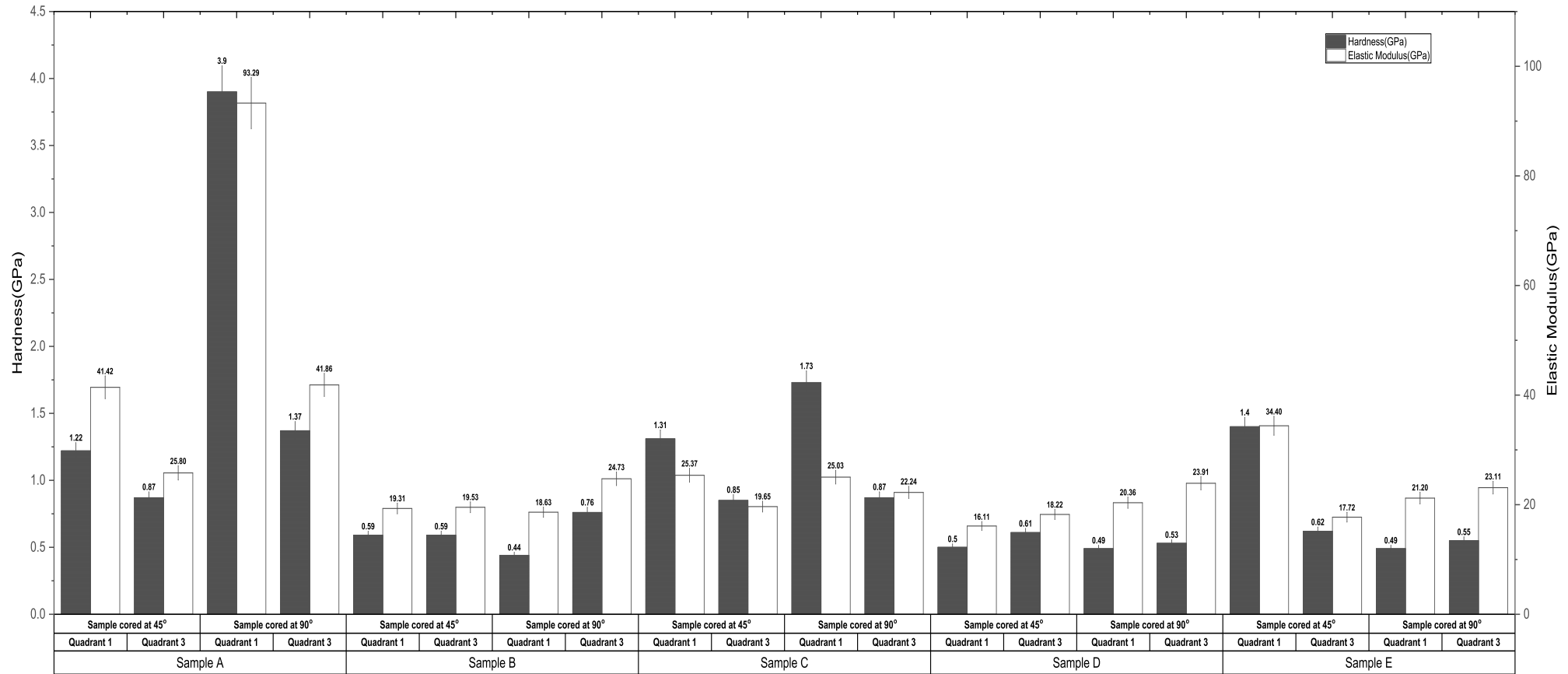
Figure 18: Comparison of Mechanical Properties of all the Samples described in section 3.1 that were tested with Micro-Indentation.

Figure 18 illustrates the proportion of hardness and elastic modulus from Micro-Indentation testing of the five samples A to E tested in quadrants 1&3 at 45° & 90° orientations to the bedding plane which compare with results from micro indentation tests conducted on Woodford Shale by Abousleiman et al. (2007) and consolidated shale drill cuttings by Martogi and Abedi (2019). Fifty indentation tests were conducted in each quadrant 1&3 as shown in Figure 3 & Figure 4. Thus for one sample one hundred indentation tests were conducted with fifty tests per quadrant.

Overall, it can be seen that the highest proportion of hardness and elastic modulus are seen in sample A cored at 90° to the bedding plane in quadrants 1&3. Furthermore, a significant variation in hardness and elastic modulus is observed in all the quadrants for each sample and orientation. It can be seen that the properties change in each quadrant but it is also a function of which orientation is tested. Samples cored at 90° to the bedding showed significantly higher hardness and elastic modulus in all the quadrants than samples cored at 45° to the bedding. This demonstrated that same material can exhibit different characteristics depending on which orientation is tested. This is attributed to the orientation of the natural fractures to the bedding and mineralogy which play a significant role in governing plasticity. Additionally, we have to consider that the fracturing process causes a damage zone due to the fluid injection that leads to a change in material properties where clay swelling can occur leading to a reduction in strength and elastic modulus. This heterogeneity can be seen in the spatial distribution of the mechanical properties seen in Figures 19, 20, 21, 22, 23. Figures 19, 20, 21, 22, 23 illustrate the hardness and elas-

tic modulus distribution in each quadrant per sample based on the orientation tested. The yellow regions indicate high hardness and elastic modulus along the area tested. These 2D hardness and elastic modulus distribution maps were constructed based on the indentation area of 4mm × 2mm shown in Figures 3& 4.

Hardness describes how a material behaves in the presence of a harder surface under a particular load and, as such, is significant when determining proppant embedment because it delineates the surface properties. The variability in the values shown in Figure 18 is attributed to the; discontinuities in formation, heterogeneity of the mineral composition, and the fluid contact during hydraulic fracturing. From Figure 18, it is clear that Sample B has the least hardness and elastic modulus values implying that samples in this zone are more susceptible to proppant embedment followed by sample E, sample D, sample C as compared to sample A which had the highest hardness and elastic modulus implying that the possibility of proppant embedment is minimal due to the high surface hardness and a higher elastic modulus. It is certainly worth noting that these findings agree with the spatial distribution maps shown in Figures 19, 20, 21, 22, 23.

With a lower rock elastic modulus, the optimal proppant packing ratio will increase, and the permeability correction factor will be lower. This is because when the elastic modulus of the rock is smaller there is a large susceptibility to proppant embedment and a lower proppant elastic modulus presented more proppant deformation. Both of these parameters reduce the fracture aperture (Liu et al., 2021; Mueller and Amro, 2015).
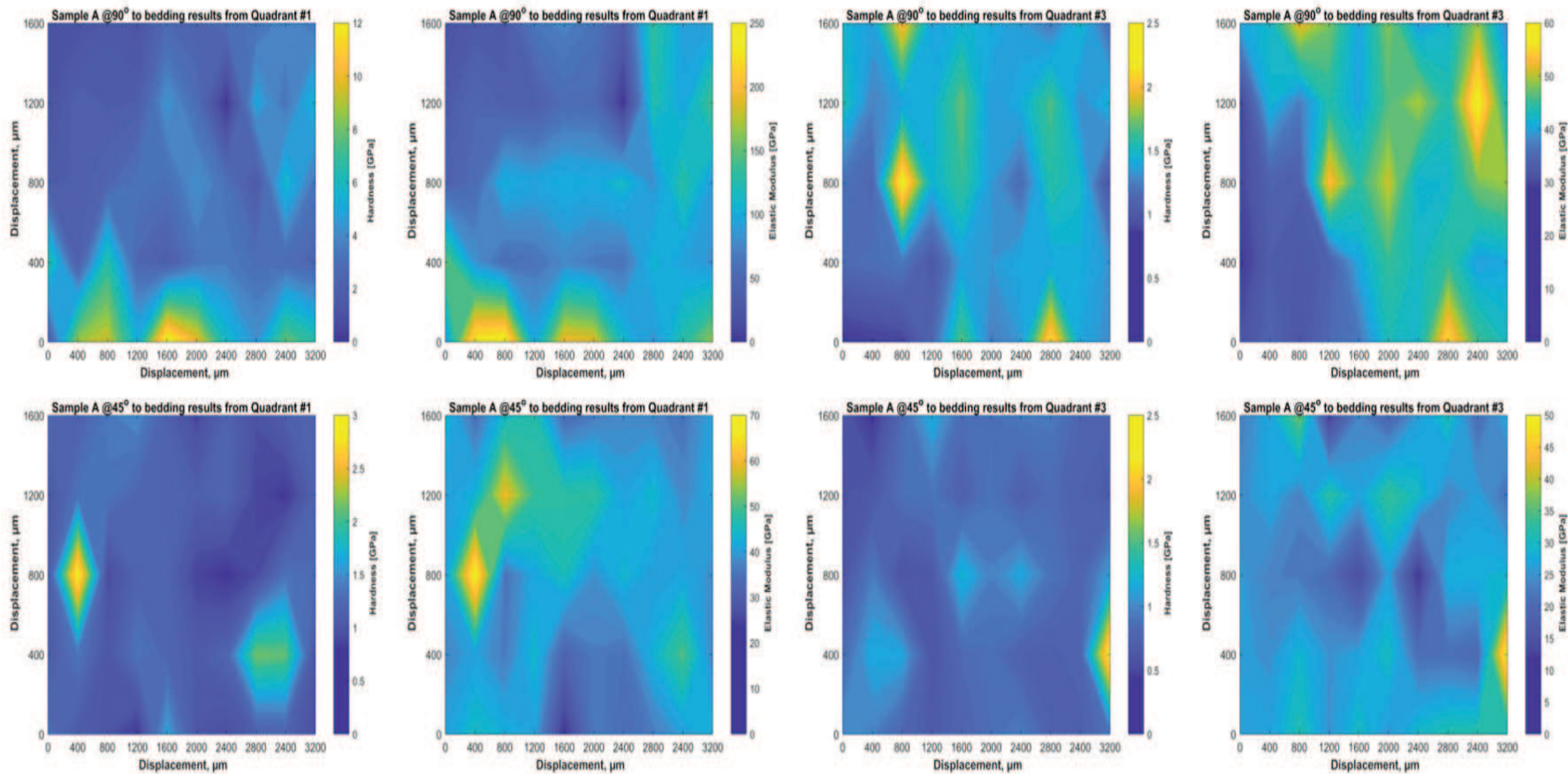
Figure 19: Maps showing the Spatial distribution of the Mechanical Properties from Sample A. Sample A is annotated in Table 1 under section 3.1.
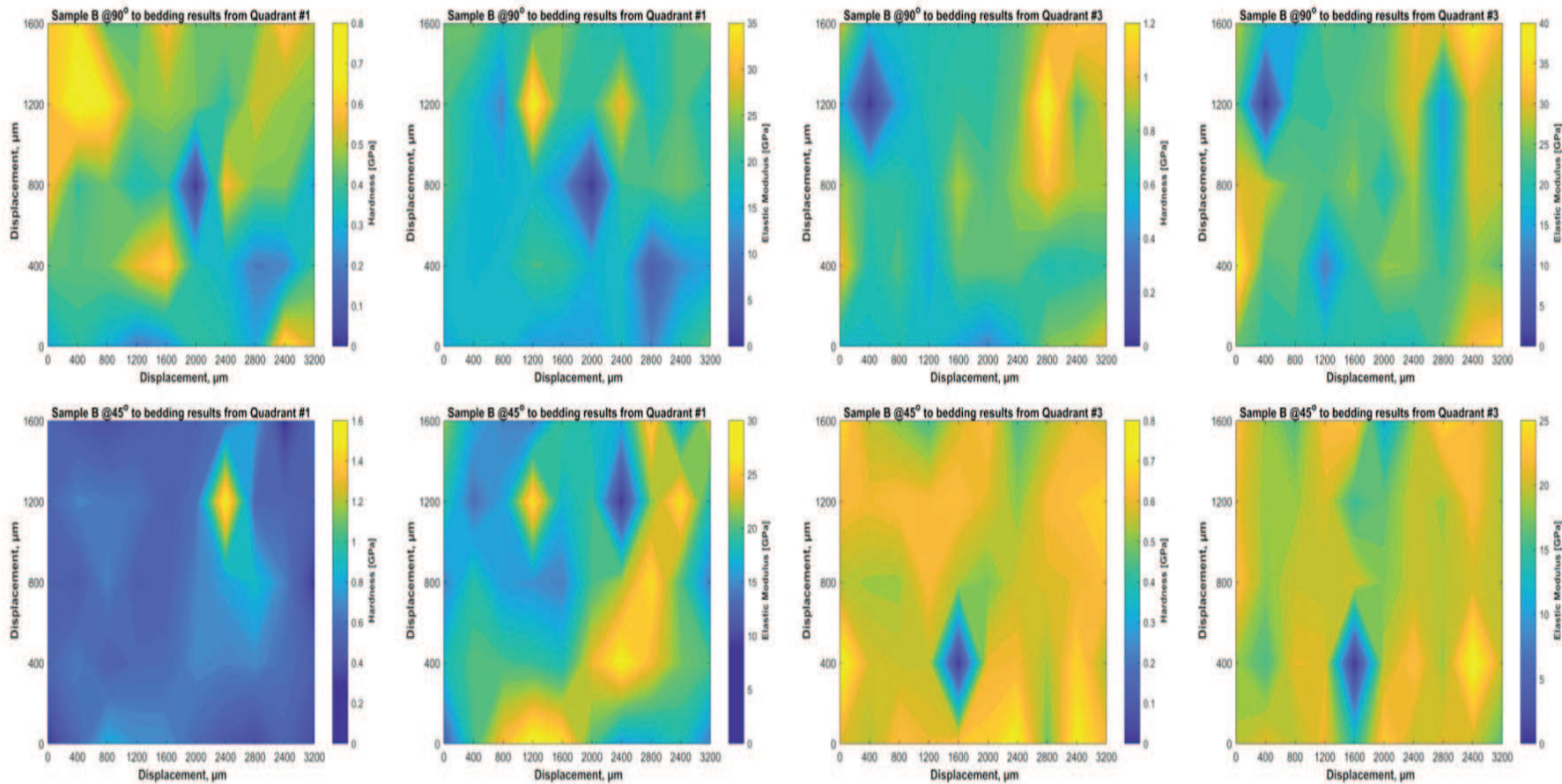
Figure 20: Maps showing the Spatial distribution of the Mechanical Properties from Sample B. Sample B is annotated in Table 1 under section 3.1.
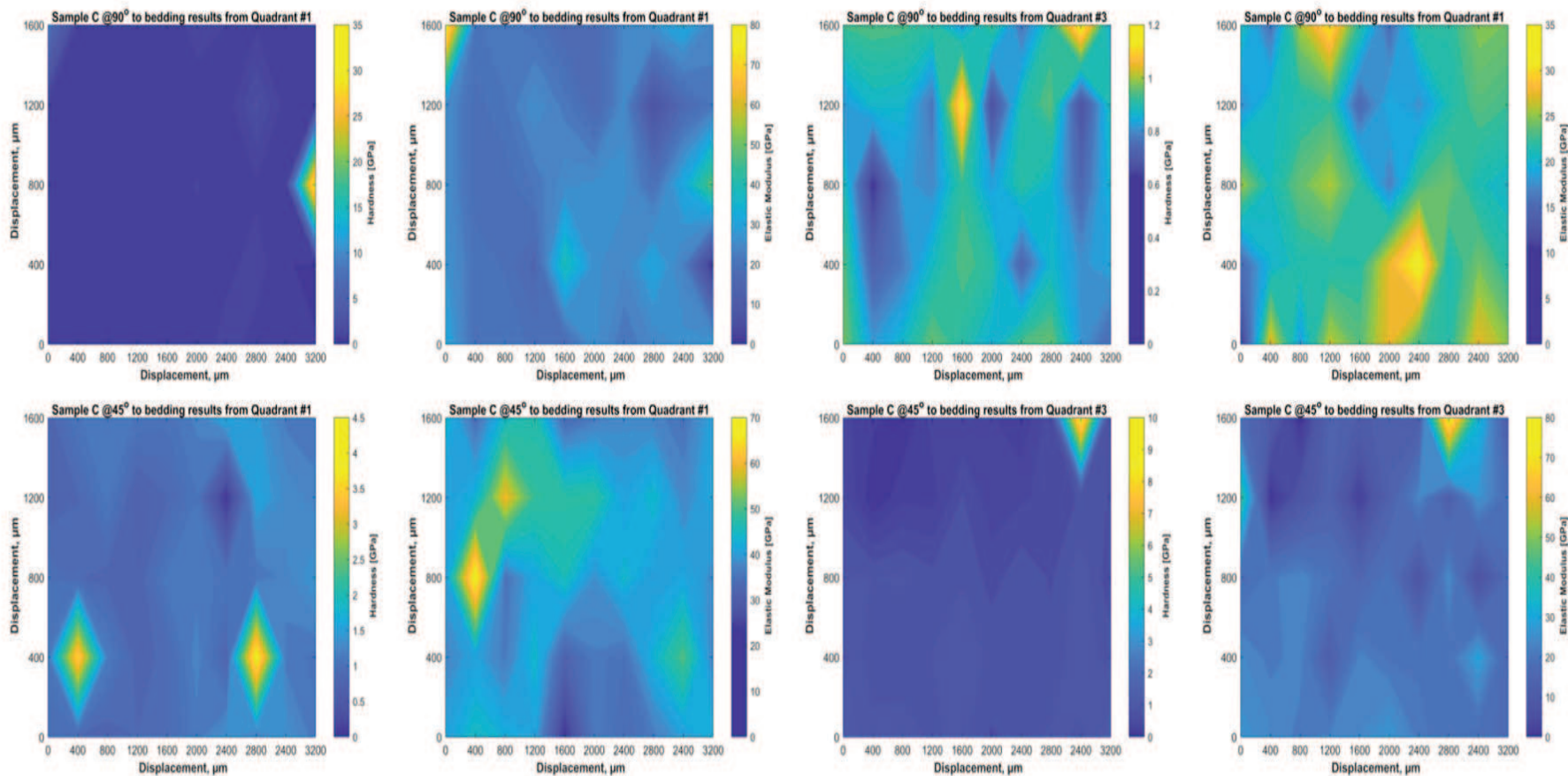
Figure 21: Maps showing the Spatial distribution of Hardness and Elastic Modulus from Sample C. Sample C is annotated in Table 1 under section 3.1.
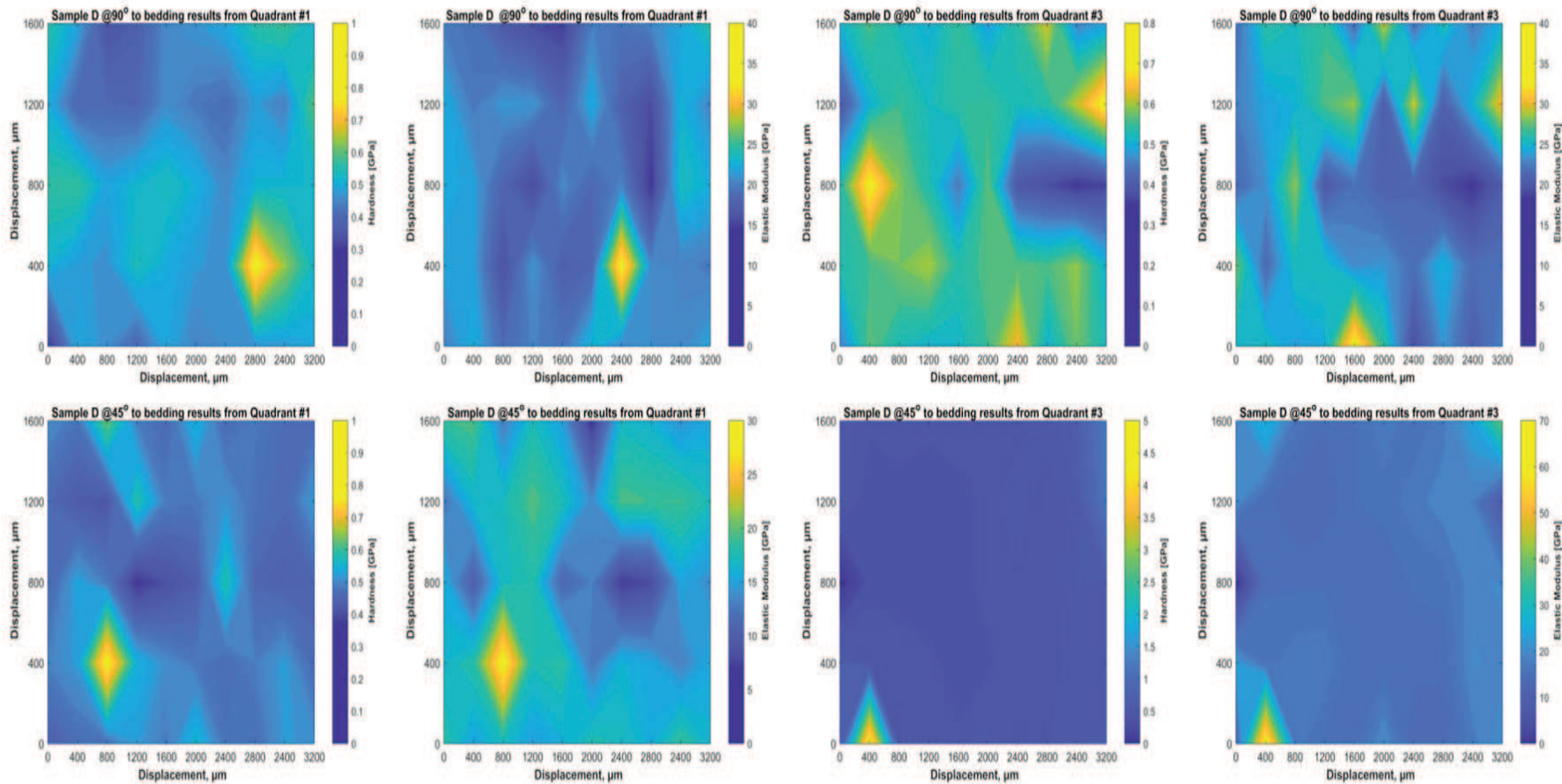
Figure 22: Maps showing the Spatial distribution of of Hardness and Elastic Modulus from Sample D. Sample B is annotated in Table 1 under section 3.1.
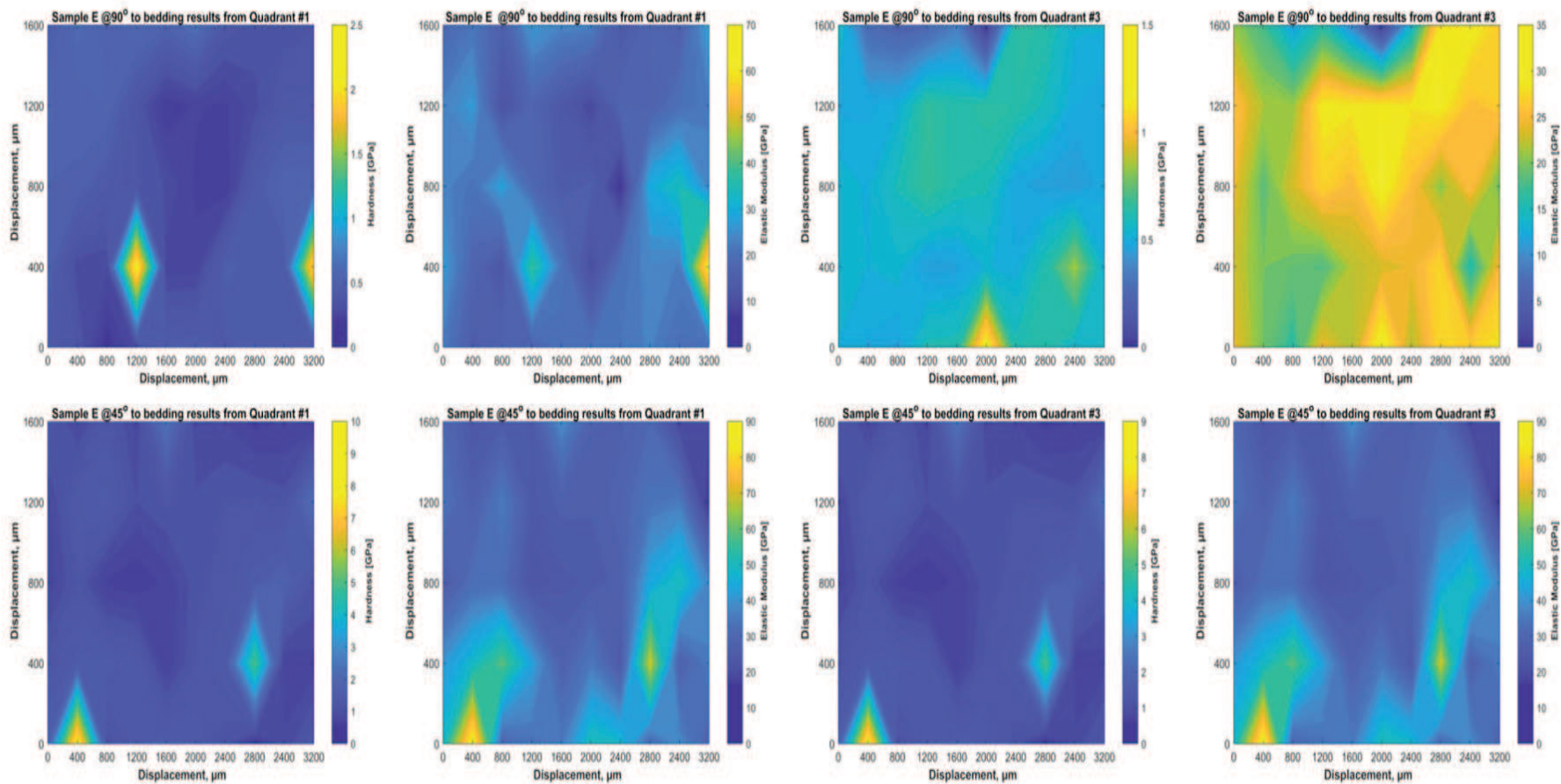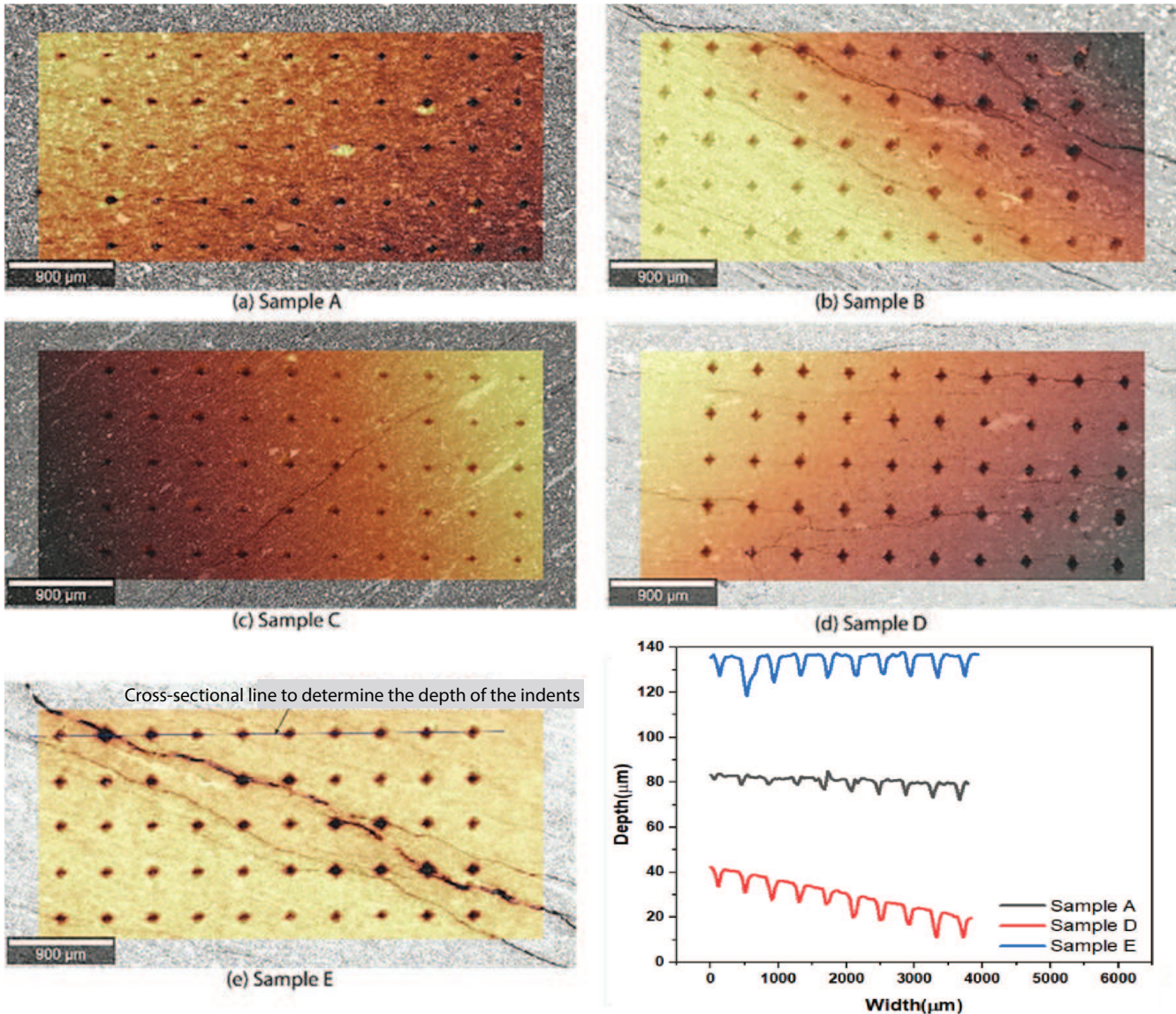
Figure 23: Maps showing the Spatial distribution of Hardness and Elastic Modulus from Sample E. Sample E is annotated in Table 1 under section 3.1.

694 *4.5. Surface Profilometry of the Samples after indentation*

Figure 24: Surface profilometry of the Caney Shale samples described in section 3.1 after indentation (a)Sample A, (b)Sample B, (c)Sample C, (d)Sample D, (e)Sample E, (f)Depth versus width of the first row along the cross sectional line drawn on samples A, D&E to illustrate how the indentation depth can vary on every indent per sample.

695 Figure 24 shows the surface profilomentry conducted in
696 Quadrant 3(See Figure 2(c)) of all the samples after inden-
697 tation. Overall, Sample A shows smaller indents compared
698 to all the samples. The smaller the indents the harder the
699 sample and thus higher hardness and elastic modulus. This
700 is also seen in Figure 18 where Sample A had the highest
701 hardness and elastic modulus compared to all the samples.
702 Micro-fractures are seen in Samples: B,C,D and E. Sample
703 E had the largest visible fractures and the largest visible in-
704 dents indicating that the surface is soft and thus the hardness
705 and elastic modulus are low compared to all other samples
706 as seen in Figure 24. This hardness and elastic modulus
707 variation is attributed to clay mineralogy and bedding ori-

708 entation. Samples that had the highest content of clays had
709 the least reported hardness and elastic modulus values com-
710 pared to sample with the least amount of clays.

711 Furthermore, to investigate the shale rock proppant in-
712 teraction after indentation was done, surface profilomentry
713 was done on the first row of indents in Sample E. The results
714 show that the indentation depths are different along each in-
715 dent which is attributed to the variation in composition of
716 the rock fabric. The variation in composition of the rock
717 fabric implies that proppants will interact differently along
718 the surface of the same material and as such a variation in
719 the degree of proppant emebedment is expected.

5. Modeling of indentation tests and proppant embedment

5.1. Elasto-plastic parameters from micro-indentations

In this section, we apply numerical modeling to investigate the potential for evaluating elasto-plastic shale parameters from the micro-indentation tests. The numerical modeling of these experiments is part of an ongoing effort to improve coupled multiphase fluid flow and geomechanical modeling of proppant-filled fractures during hydrocarbon production. The necessary model developments and applications are based on the linking of the TOUGH2 multiphase flow simulator with the FLAC3D geomechanical simulator (Itasca, 2011; Pruess et al., 2012; Rutqvist, 2017). For the modeling of the micro-indentation tests, the FLAC3D geomechanical simulator is applied with detailed modeling of the Vickers pyramid indenter and its contact with the shale surface.
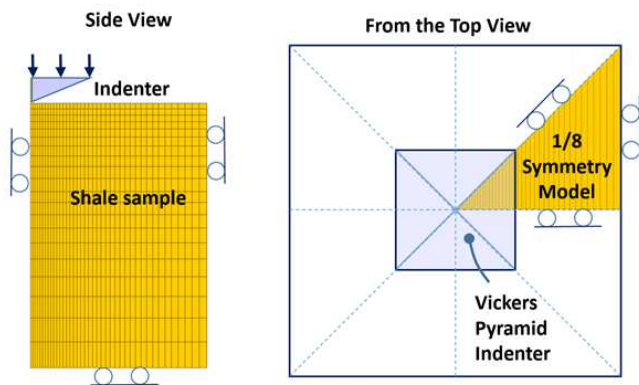

Figure 25: Numerical model of the micro-indentation tests

The geometry of the Vickers pyramid-shaped indenter allows for modeling the experiment using a 1/8 symmetric model of the full 3D geometry (Figure 25). The rollers in Figure 25 illustrate boundaries where displacement is allowed parallel to the boundary surface while no displacement is allowed normal to the boundary. On top of the indenter, vertical velocity is imposed to first pressure the indenter downwards to a desired indentation depth. Once the depth is reached, the vertical velocity is reversed to unload the indenter. The diamond indenter is modeled as an elastic material with a Youngs modulus of 1040 GPa and Poissons ratio of 0.07, i.e. a very stiff material compared to the shale samples. Figure 25 also shows the mesh discretization. The mesh was refined near the indenter tip until to such a degree that smooth load-indentation curves were achieved from the first instant of indenter touching the simulated shale sample.

We adapted an elasto-plastic Mohr-Coulomb model that was subsequently applied to model proppant embedment in shale fractures under field conditions. The application of a Mohr-Coulomb model for the interpretation of indentation in ductile shale was recently demonstrated in Voltolini et al. (2021) involving high-resolution X-ray micro-imaging of strain. The modeling of the indentation experiment in Voltolini et al. (2021) showed that different combinations of cohesion and internal friction angle could be used in a model to match the experimental load-indentations curves of the type shown in Figure 26a. However, modeling of the strain field as observed from the X-ray micro-imaging could be used to further constrain the values of cohesion and friction angle. For the micro-indentation tests on the Caney shale we model the loading and unloading curves and the observed indentations pattern. We also compare the elasto-plastic properties used for the modeling of the micro-indentation tests with those evaluated from triaxial compression experiments on core-samples. In fact, the cohesion and internal friction angle as well as the Young's modulus and Poisson's ratio evaluated from previous core-scale laboratory experiments are used as an initial parameter set. The triaxial core-scale compression experiments were performed at the University of Pittsburgh and the results include the parameter values listed in Table 2. The actual experimental data provide Young's modulus and Poisson's ratio at different confining stress levels, while in this modeling study we used the average values that are listed in Table 2.

Table 2: Elasto-plastic material properties for five Caney shale formations evaluated from triaxial compression tests at the University of Pittsburgh. These parameter values were used as a starting set of parameters in the modeling of the micro-indentation tests.

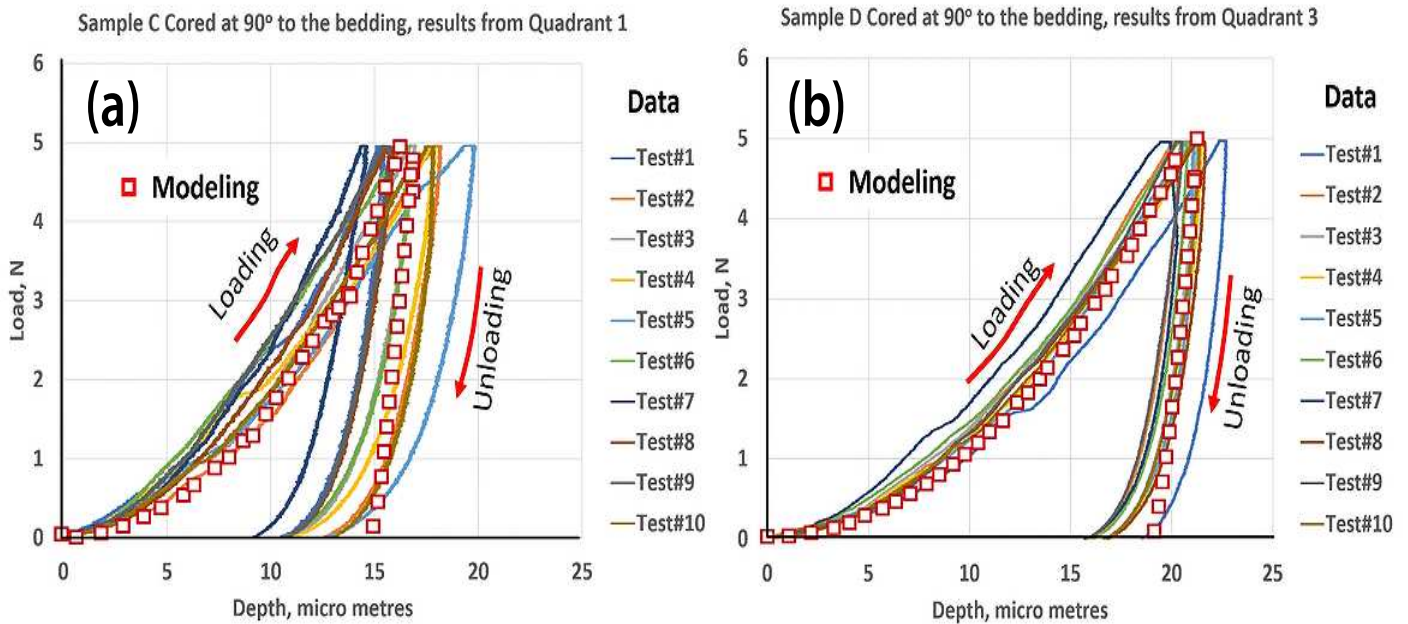| Formation	Young's Modulus (GPa)	Poisson's ratio (-)	Cohesion (MPa)	Internal friction angle (^{o})
Reservoir 1 (Sample A)	25.6	0.19	27.2	25.1
Ductile 1 (Sample B)	26.2	0.2	16.8	34.4
Reservoir 2 (Sample C)	23.3	0.2	10	49.7
Ductile 2 (Sample D)	20	0.15	22.5	25.9
Reservoir 3 (Sample E)	26.8	0.17	60.4	4.6

Figure 26: Experimental load-indentation curves for (a) Sample C and (b) Sample D with modeled load-indentation curves using elasto-plastic parameters listed in Table 2.

781 Figure 26 shows two examples of simulated load-
782 indentation curves overlain on top of a number of experi-
783 mental load-indentation curves. The model simulations are
784 performed with the properties listed in Table 2 for Sample
785 C and D properties, which represent two formations with
786 markedly different clay content. The results show that the
787 modeling using the elasto-plastic parameter evaluated from
788 the triaxial core-scale compression tests provides modeled
789 unload-loading curves that are within the range individual
790 indentation experiments on each formation. Such an agree-
791 ment shows consistency between the elasto-plastic param-
792 eters from micro-indentation and core-scale experiments.
793 The range of the micro-scale load-indentation curves for
794 each formation can be attributed to micro-scale heterogene-
795 ity of the shale samples. The simulated indentation tests
796 show a maximum indentation depth of respective 16μm and
797 21μm and corresponding hardness of about 2 and 0.5 for
798 Sample C and D models. A much smaller indentation depth
799 for Sample C modeling can attributed to a much higher
800 friction angle. A high friction angle have a high impact
801 on strength at high confining stress. The modeling results
802 show that the very high stress of hundreds of mega-Pascals
803 develops in the shale samples just below the indenter, in-
804 cluding high values of all three principal stresses. The sim-
805 ulated load-indentation curves for Samples A, B and E do

806 also fall within the range of experimental load-indentation
807 curves. However, the simulation results for Sample E de-
808 viate in terms of the shape of the indentation pit with a
809 significant pile-up at the edge of the indentation pit (Fig-
810 ure 27a). Such a significant pile-up can occur for the com-
811 bination of a low friction angle ($\phi = 4.6^o$) and high cohesion
812 ($C = 60.4$) that were used as an initial parameter set based
813 on the core-scale experiments. If we apply an alternative
814 pair of strength parameters with higher friction angle ($\phi =$
815 30°) and a lower cohesion ($C = 18$) no significant pile-up
816 is calculated (Figure 27b). This alternative pair of strength
817 parameters was determined by calibrating the cohesion for
818 a fixed friction angle ($\phi = 30^o$) until the approximated load-
819 indentation curve matches the load-indentation curve for the
820 original strength parameters. Thus, the simulations with the
821 two sets of parameters ($\phi = 4.6^o$ with $C = 60.4$ and ($\phi = 30^o$
822 with $C = 18$) results in identical load-indentation curves but
823 a significant difference in pile-up adjacent to the indenter
824 (Figure 27). The depth profiles from the experiments shown
825 in Figure 24 does not indicate significant pile-up for Sample
826 E. Therefore, the model parameters with $\phi = 30^o$ and $C = 18$
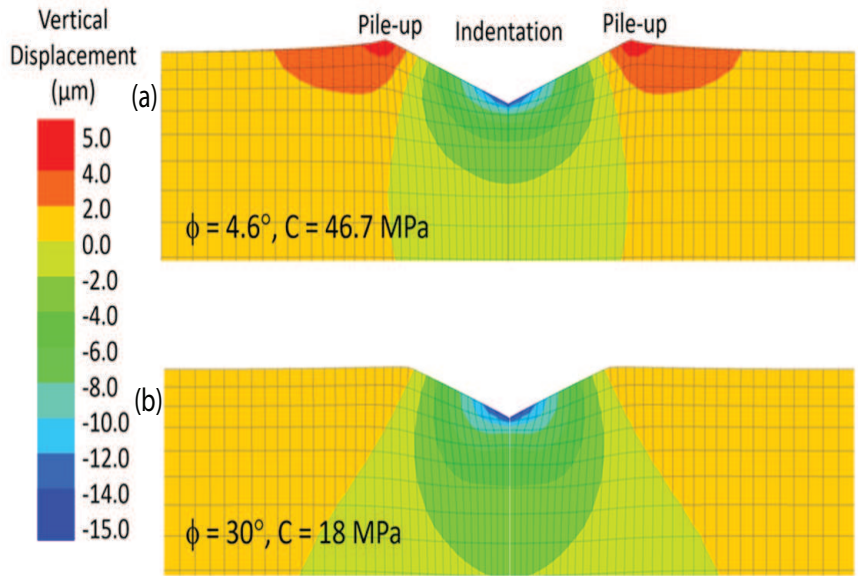827 seems to better match with the Sample E micro-indentation
828 data.

Figure 27: Modeled indentation pit for two alternative Sample E properties after unloading.

5.2. Modeling of elasto-plastic proppant embedment

Susceptibility to proppant embedment is assessed by numerical modeling using the Mohr-Coulomb elasto-plastic material parameters that were evaluated from the modeling of the micro-indentation tests in Section 4.5. Here we conduct modeling using properties for Samples C and D, where Sample D represents a formation with higher clay content and weaker strength properties. We consider a fracture closure stress of 10,000 Psi (72 MPa), which is estimated for a depth of about 14200 feet(3400 m) in Oklahoma (Vulgamore et al., 2008). Moreover, we consider the potential embedment of an ideal spherical proppant of 0.5 mm (500μm) in diameter. The load taken by one proppant from the fracture closure stress will depend on the spacing between neighboring proppants in a monolayer and will depend on the reservoir pressure. The modeling is performed using an axial symmetric model, similar to that for the micro-indentation tests, but considering the spherical shape of the proppant (Figure 28). An average spacing, or center-to-center distance, between individual proppants are simulated by changing the radius of the axisymmetric model. The rollers in Figure 28b illustrates boundaries where displacement is allowed parallel to the boundary surface while no displacement is allowed normal to the boundary. A vertical force is applied on top of the half proppant model. The model results are visualized by assembling the axisymmetric model as shown in Figure 28c considering repetitive symmetry depicted in Figure 28a.

(a) Plane view of proppant distribution
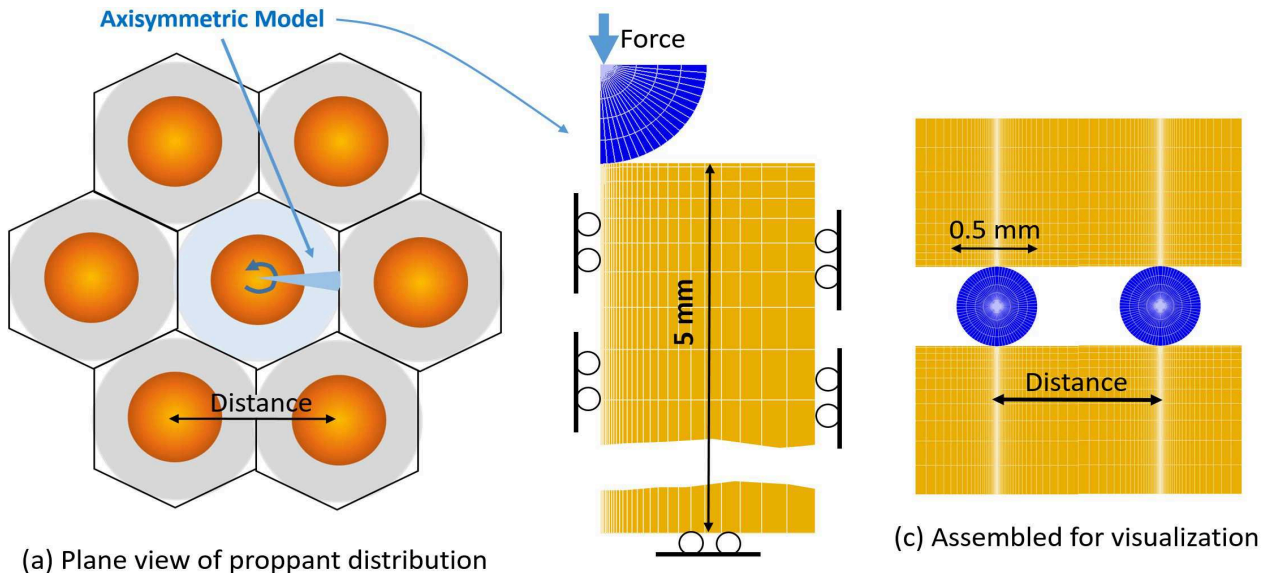
(c) Assembled for visualization

Figure 28: Axisymmetric model for simulation of proppant embedment and fracture closure for a distribution of proppants at a uniform center-to-center distance. .
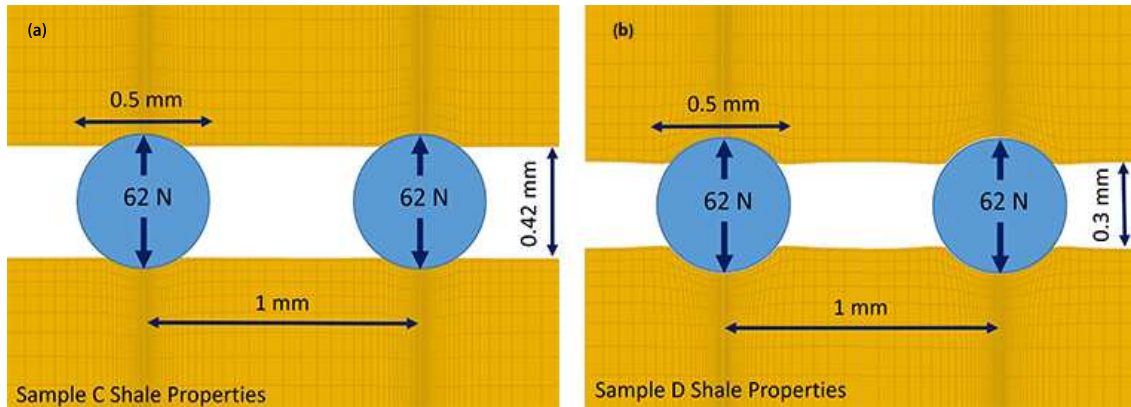
Figure 29: Modeled proppant embedment due to elastic and plastic shale deformation for (a) Sample C and (b) Sample D shale properties and proppant center-to-center spacing of 1 mm.
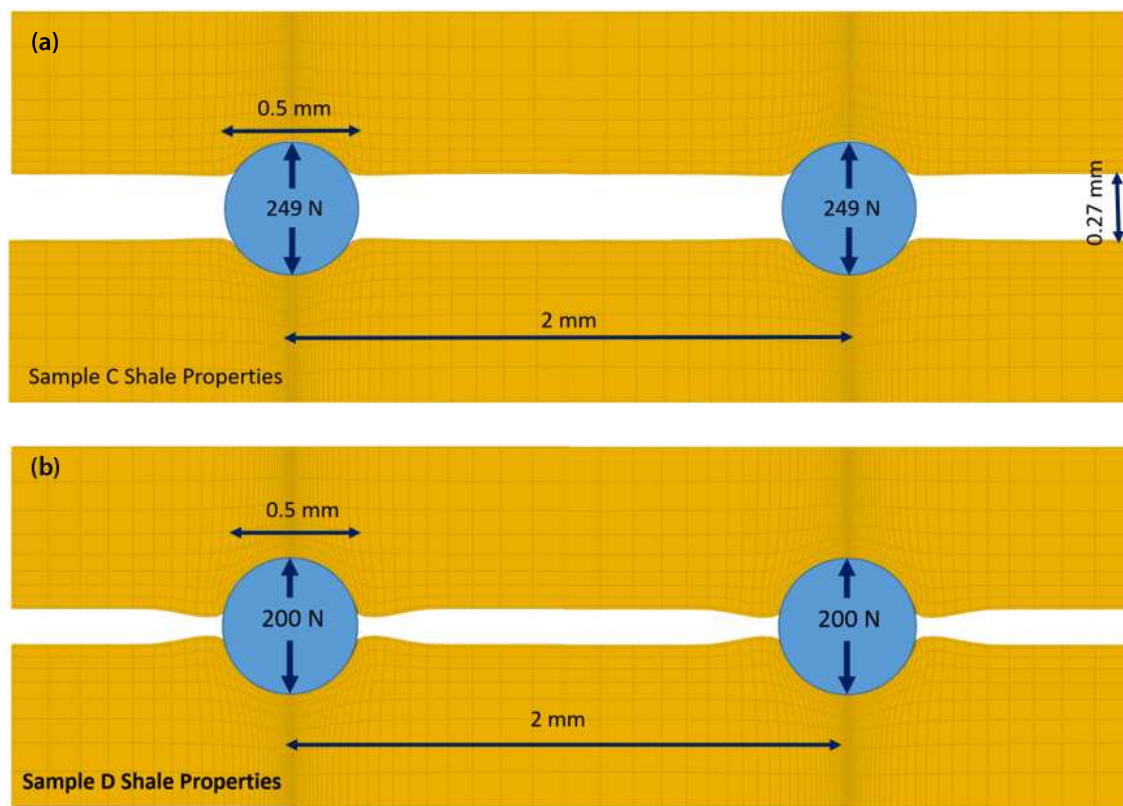

Figure 30: Modeled proppant embedment due to elastic and plastic shale deformation for (a) Sample C and (b) Sample D shale properties and proppant center-to-center spacing of 2 mm.

Figure 29, Figure 30 present modeling results of embedment for two different idealized cases involving 0.5 mm (500μm) diameter proppants located at center-to-center distances of respectively 1 mm and 2 mm. While this spacing between grains is arbitrarily selected, it serves a specific purpose which is to illustrate the sensitivity of the results to this detail of the proppant distribution. In the case of a 1 mm center-to-center distance, the calculated average load on a proppant is estimated to be 62N for an extreme case of complete pressure depletion due to fluid production (Figure 29). The proppant embedment is calculated to about 40μm for Sample C properties and 100μm (0.1 mm) for Sample D properties. Thus, the fracture aperture between proppants would be about 420μm (0.42 mm) for Sample C properties and 300μm for Sample D properties. Considering the case of a 2 mm center-to-center distance between proppants, the average load on one single proppant is estimated to be 249N (Figure 30). In the case of Sample C properties, the proppant embedment for 249N proppant load is about 115μm (0.115 mm), with a remaining aperture of 270μm (0.27 mm). In the case of Sample D properties, a complete embedment of the proppant and closure of the fracture occurred at a proppant load of about 200N, which is well below the estimated maximum load of 249N upon complete pressure depletion.

The modeling demonstrates the importance of plastic de-

formation and plastic strength properties for proppant embedment as localized shear failure in the shale just below the proppant-shale contact can accommodate embedment. We applied a Mohr-Coulomb model with parameters obtained from core-scale experiments and validated against micro-indentation tests. The modeling reveals a significant difference in proppant embedment behavior for Sample C and D properties. Note that individual micro-indentation tests showed strongly heterogeneous load-indentation behavior, indicating significant local variability of hardness and elastic modulus. The two cases presented in Figure 30(a) and Figure 30(b) for Sample C and D properties correspond to hardness values of about 2 and 0.5. In the field, heterogonous shale properties would lead to a fracture held open by proppants located at more competent fracture wall rock. However, high load concentration at those locations could be prone to crushing and local fracturing at the shale-proppant contact. ==Effect of shale micro-scale heterogeneity on proppant-filled fractures will be included in future modeling efforts. Moreover, longer term proppant embedment during production can involve a significant creep deformation, a process that will be studied in future research within the Caney Ductile Shale Project. Still, even with the limitations of scope in the present work, it is clear that proppant embedment can vary significantly among the formations and, of practical relevance, that achieving close proppant packing is important for limiting proppant embedment, especially in weaker formations.==

6. Discussions

6.1. The effect of clay mineralogy

Variations in the microstructure and mechanical properties illustrated in Figure 18 indicate the amount of total clays present, which correlates with the mineralogical analysis. It is therefore necessary to directly delineate the type of clay, and the impact of its properties; for instance, swelling, shear resistance and shrinkage.
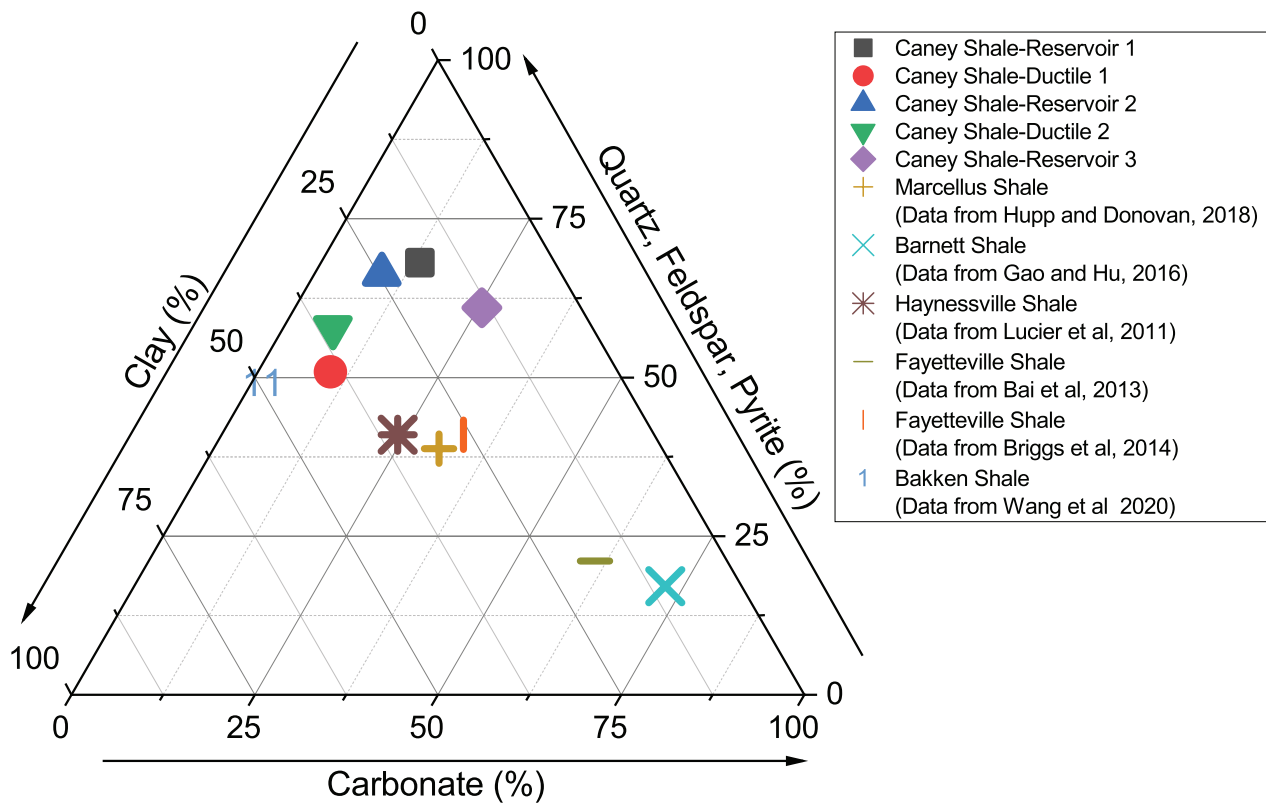

Figure 31: Illustration of the Mineralogical Composition of the Caney Shale in comparison to other producing Shale formations

Overall, mineralogical composition for these five zones of interest is shown in Figure 31, separating reservoir sections, from ductile sections, primarily by amount of clays present. This is also in comparison with other producing shale plays such as: Marcellus (Hupp and Donovan, 2018), Barnett (Gao and Hu, 2016), Haynessville (Lucier et al., 2011), Fayetteville (Bai et al., 2013; Briggs et al., 2014) and Bakken Shale (Wang et al., 2020). The Caney Reservoir sections (1, 2 and 3) have from 13.5 to 18.4% total clays, while Caney ductile regions have more than double the amount of clay fraction, up to 38%, when compared to reservoir samples. The swelling and shrinkage effect often results in a reduced strength bearing capacity. Josh et al. (2012, 2019) demonstrated that the strength of the shale corresponds with both the cation exchange capacity(CEC) and the content of the silt. As such, clays have anisotropic properties that are intrinsic and caused by stress. Dielectric constants are related to water content, and the dispersion in dielectric constants depends on the CEC of clays and strength of the rock. The orientation of the micro-fabrics with respect to bedding planes was found to be a critical factor in stress-induced anisotropy. Pachytel et al.

(2017) have studied the influence of calcite on mineralogical composition. The results of the study revealed that the carbonates showed a more significant effect on the influence of the elastic modulus and the brittleness index than quartz. Yakaboylu et al. (2020) examined the deformation and microcracking behavior of the Marcellus shale through micro-strain analysis. They tested samples that were cored perpendicular and parallel to the bedding. Sample mineralogy was quantified using X-ray diffraction(XRD) and XRD peak shapes were analyzed using the William Hall approach, demonstrating higher concentrations of lattice defects and associated in-homogeneous crystallographic strain in calcite than in quartz. The parallel-bedded shales also indicated more micro-strain than the perpendicular-bedded shales. The results indicate that micro-cracking initiation and propagation, as well as mechanical deformation of calcite minerals, are dependent on micro-strain level and bedding orientation.

6.2. The effect of bedding orientation

A large number of researchers (Antinao Fuentealba et al., 2020; Goral et al., 2020; Heng et al., 2020; Holt et al., 2020; Hou1 et al., 2019; Islam and Skalle, 2013; Lu et al., 2021; Minardi et al., 2021; Sone and Zoback, 2013a,b; Yin et al., 2019) have endeavored to delineate the key mechanical properties of shale. These studies concluded that the orientation of the sample with which the sample is cored relative to the bedding plane influences the mechanical parameters obtained. The variation in the mechanical parameters obtained illustrated in figure 18 can be attributed to the possibility that the cracking characteristics might differ as the orientation changes. Many fabrics are parallel to bedding planes which are produced by platy clay minerals deposition (Heng et al., 2020; Islam and Skalle, 2013). The lateral cracks propagate along these fabrics when the core samples are retrieved at 90° and 45° to the bedding planes, leading to the formation of a chipping-dominated crack geometry adding complexity to a myriad of natural fractures that is already existent and observed at the micro-scale with SEM in figures 10, 11, 12. When indentation is conducted on samples cored perpendicular to the bedding planes, this may facilitate the propagation of axial cracks. Once there are dominant axial cracks, the elastic energy will be released, and the stress concentration will be reduced at the edges of the indentation impress. As a result, radial cracks will become less prevalent. Therefore, if the indentation is conducted on samples cored at 45° to the bedding planes, axial and radial crack-dominating cracks can form. This implies that the mechanical parameters that are obtained are likely to be different, and the trend in variation is likely to replicate that observed in the core-scale experiments by previous scholars. Sone and Zoback (2013a,b) examined the static and dynamic attributes and anisotropy of; Barnett, Haynesville, Eagle Ford, and Fort St. John shale rocks as they relate to mechanical properties. The results of their study show that the elastic anisotropy of shale is an outcome of the orientated deposition of clay minerals and attributes of clays. Islam and Skalle (2013) used a triaxial test including a Brazilian test, and CT scans to investigate the mechanical properties of Pierre shale cored at different orientations. The results suggested that the bedding plane and the failure plane coincide nicely, implying that the bedding plane orientation affects properties significantly. Goral et al. (2020) examined the macroscopic and microscopic properties of shale. Their outcomes showed that the behavior of Pierre shale in terms of its geomechanical properties is scale-dependent and directly influenced by structural anisotropy. The bedding planes in shale were analyzed by Heng et al. (2020) using a Brazilian test, direct shear and three-point bending tests and looking at outcrop samples from the Longmaxi Formation. Their study showed that the bedding layers are weak spots in terms of the strength of tensile tension, the strength of shear tension, and fracture toughness. This is because when fractures propagate in the direction that is normal or oblique to bedding, complex fracture geometry with tortuous propagation paths are generally caused by bedding cracks and fracture deviations toward bedding in the parallel orientation. Ibanez and Kronenberg (1993) explain that shale samples can exhibit scale fractures, bands of kink and shear zones, with the location of the fractures and the geometry of the shear zones depending on which direction the sample was cored in relative to the bedding.

6.3. The role of the microstructure

Microstructural characterization is critical for better understanding of the rock susceptibility to mechanical or chemical failure. Figures 10,11 & 12 show consistent presence of structural heterogeneity in all the SEM micrographs, which could have a major impact on the fracture initiation and propagation as well as the long-term fracture conductivity. The internal architecture of the rock matrix, primarily the solid vs pore/fracture volume, geochemical composition, mineral shape, size and packing, all can influence how rock responds to both, physical and chemical stimulation. during wellbore construction and the consequent production of fluids.

As observed in Figure 32 below, which shows an area where all constituents are present, from organic matter (OM) to fine grained clay matrix that envelops larger carbonate grains and much smaller particles of quartz, particles of sand would have very different response upon landing on each of the above-mentioned shale components. This gets further complicated as the rock is contacted by hydraulic fracturing fluid, which may cause dissolution/precipitation and formation of new materials.

Figures 10,11 & 12 have shown varying heterogeneity in all the SEM micro-graphs indicating that is vital to characterize the microstructure such that it could enable locating fracture intervals. All the physical and chemical alterations of the shale rock are time sensitive, and the evolution seems to have a negative impact, based on the field data and the prevailing decline of production in most unconventional plays after 1-3yrs (Guan et al., 2021; Lu et al., 2021; Radonjic et al., 2020; Saif et al., 2017; Voltolini et al., 2021). The goal of this study has been to characterize Caney shale core samples and based on the data predict which core samples would be susceptible to proppant embedment. From Figure 18, it is evident that sample B has the least hardness and

elastic modulus values implying that samples in this zone are more susceptible to proppant embedment followed by sample E, sample D, sample C as compared to sample A which had the highest hardness and elastic modulus imply-

ing that the possibility of proppant embedment is minimal due to the high surface hardness and a higher elastic modulus.
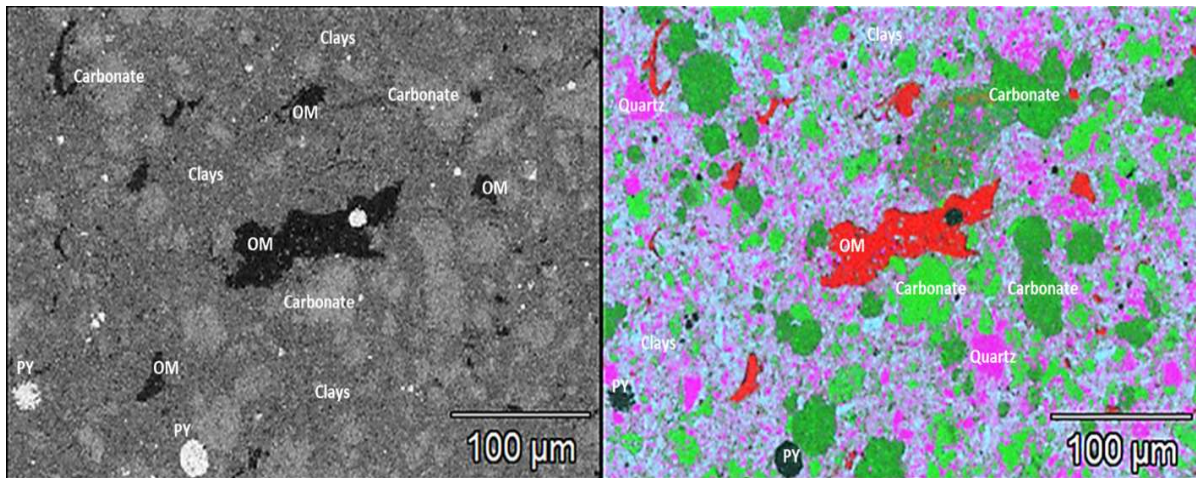

Figure 32: Backscattered Electron (BSE) micrograph (left) and the EDS map (right) obtained from a polished surface of Caney sample, show the presence of the dominant fine grained clay matrix that envelops larger carbonate grains and much smaller particles of quartz and some organic matter (OM)

7. Conclusions

The work presented in the paper has shown that amalgamating micro geochemistry and micro geomechanics can provide a synergistic workflow that can enable researchers to better understand and predict proppant embedment. This workflow can provide critical mineralogical information and microstructural characteristics of shales that can enable a better understanding of their characteristics. From this study, the following conclusions are drawn:

1. The use of surface profilometry can be useful in estimating indentation depth that help predict proppant embedment. Back Scatter Electron images have shown a pore structure that is hosted by organic matter as compared to a pore structure hosted by minerals.

2. Energy Dispersive spectroscopy can provide a better understanding in predicting the surface chemistry that is vital for proppant embedment.

3. Mineralogy, microstructural characteristics and bedding orientation play a vital role in governing proppant embedment.

4. This study has exemplified that modeling results closely followed the experimental results and demonstrated the importance of plastic deformation and plastic strength properties for proppant embedment as localized shear failure in the shale just below the proppant-shale contact can accommodate proppant embedment.

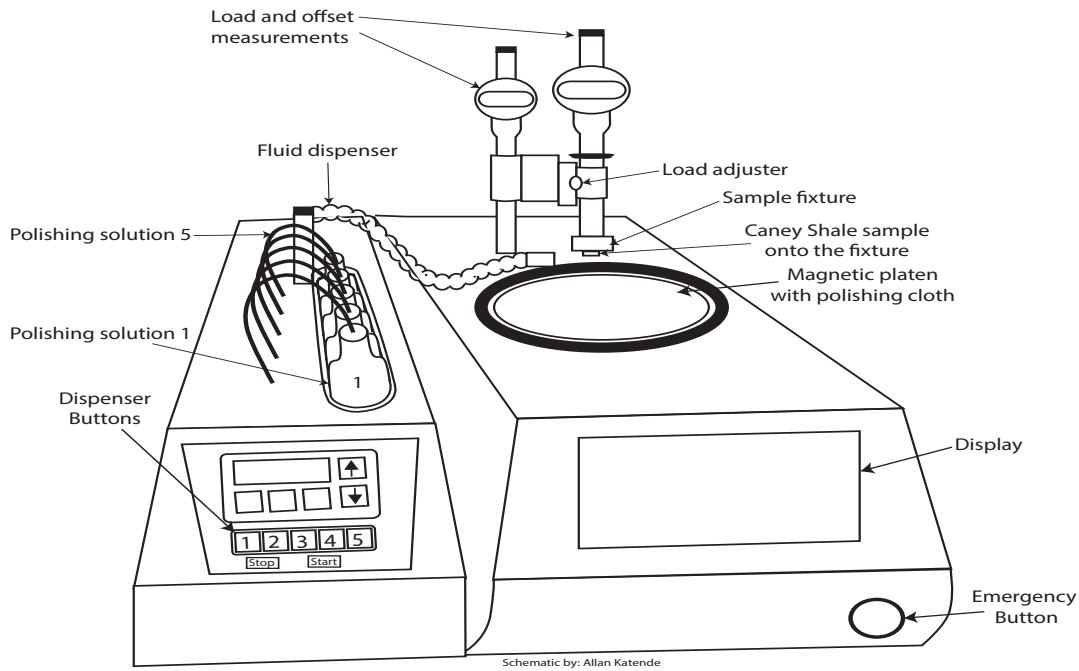**Appendix A. Sample Preparation and Analysis**

Figure A1: Schematic illustration of the polisher in the Venture I facility at Oklahoma State University Laboratory used during the sample preparation.
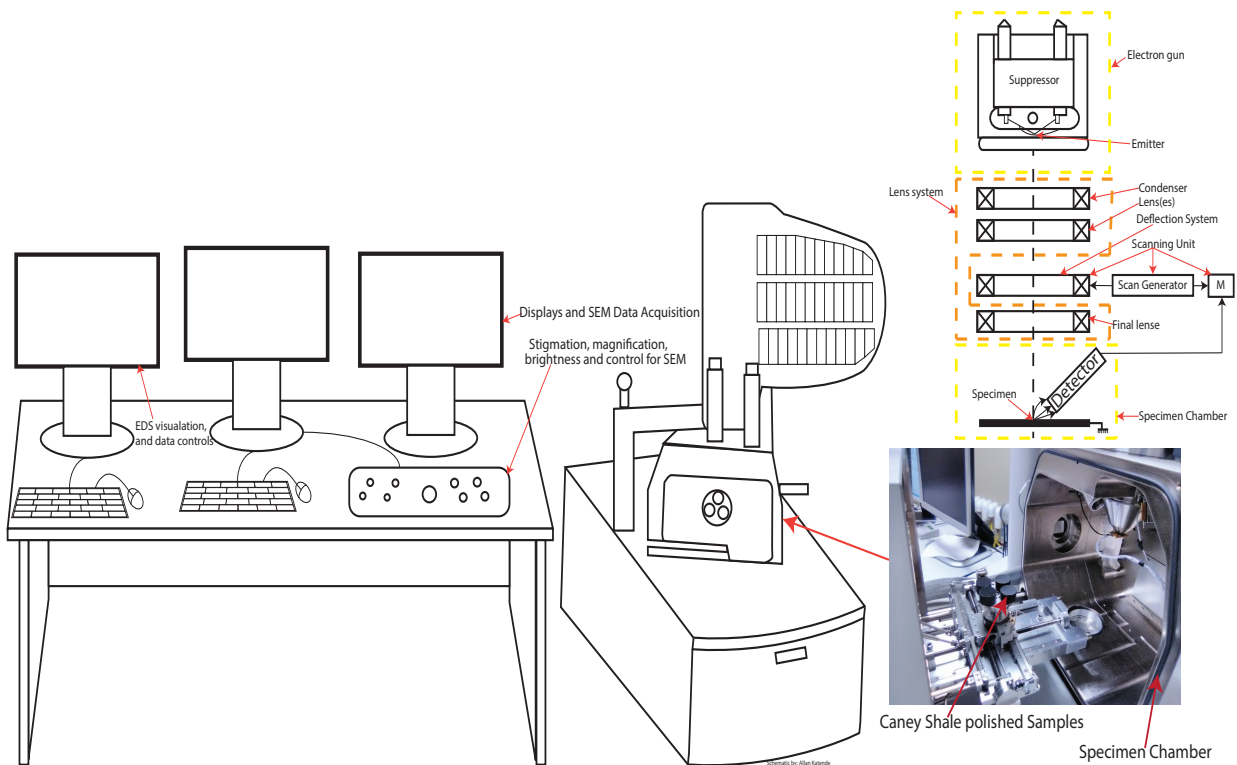

Figure A2: Schematic of the Scanning Electron Microscope set-up in the Venture I facility at Oklahoma State University Laboratory used during the sample analysis.
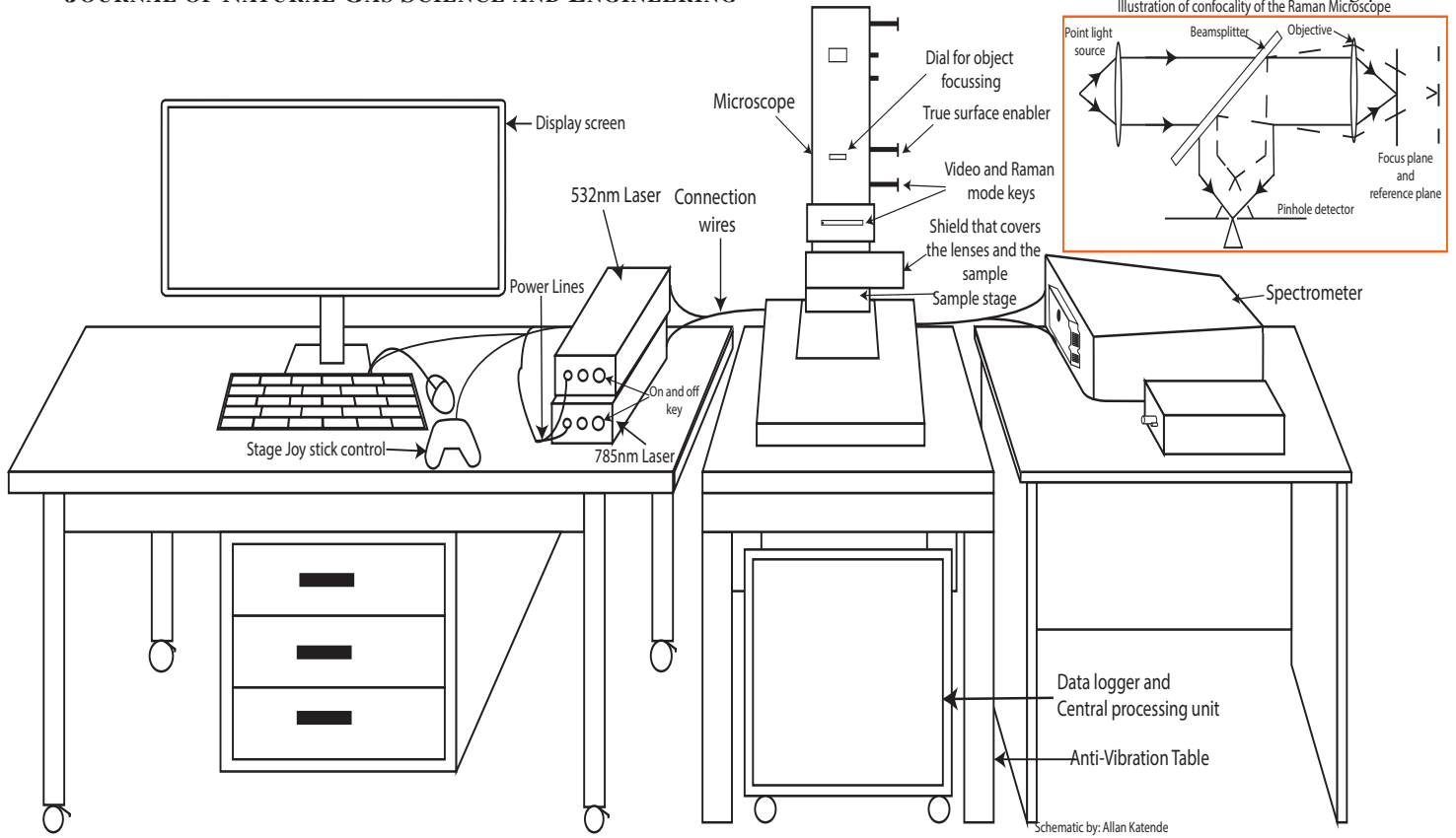
Figure A3: Schematic of the Raman microscope in the Hydraulic Barrier Materials Laboratory at Oklahoma State University (Katende et al., 2021).
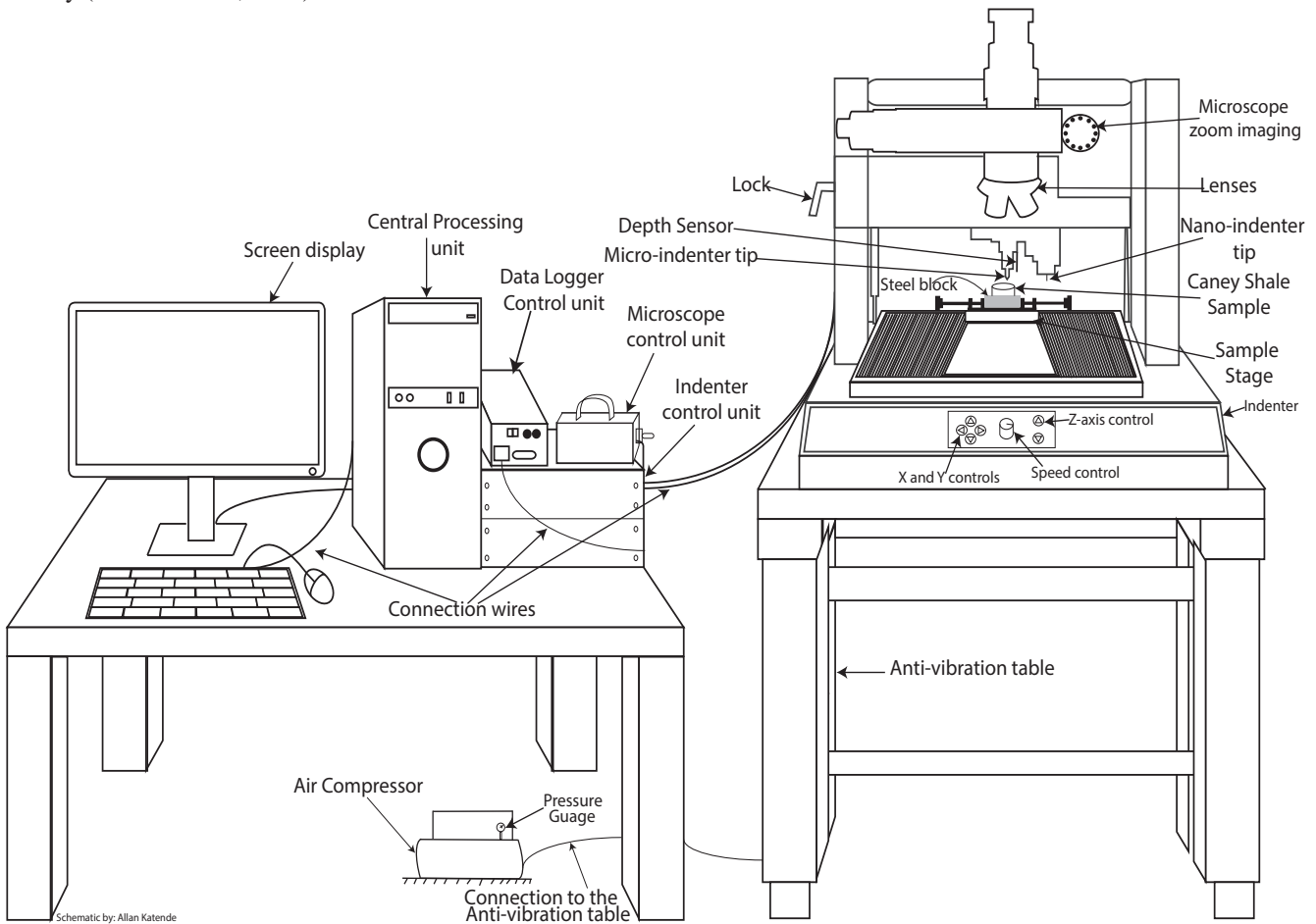

Figure A4: Schematic of the Indenter in the Hydraulic Barrier Materials Laboratory at Oklahoma State University (Katende et al., 2021).

Bibliography

Y. N. Abousleiman, M. H. Tran, S. Hoang, C. P. Bobko, A. Ortega, and F.-J. Ulm. Geomechanics Field and Laboratory Characterization of the Woodford Shale: The Next Gas Play. pages 1–14. SPE Annual Technical Conference and Exhibition, 11-14 November, Anaheim, California, U.S.A., 2007. doi: 10.2118/110120-MS.

P. Allix, A. Burnham, M. Herron, and R. Kleinberg. Oil Shale, and Oil-Bearing Shale: Similarities and Differences. AAPG Search and Discovery, 2010.

T. I. Anderson, B. Vega, and A. R. Kovscek. Multimodal imaging and machine learning to enhance microscope images of shale. Computers & Geosciences, (104593,2020), 2020. doi: 10.1016/j.cageo.2020.104593.

G. D. Andrews, S. R. Brown, J. Moore, D. Crandall, and P. Mackey. The transition from planar to en echelon morphology in a single vein in shale: Insights from X-ray computed tomography scanning. Geosphere, 16(2):1–14, 2020. doi: 10.1130/GES02191.1.

R. D. Andrews. Stratigraphy, Production, and Reservoir Characteristics of the Caney Shale in Southern Oklahoma. The Shale Shaker, 58(1):9–25, 2007.

R. D. Andrews. My Favorite Outcrop - Caney Shale Along the South Flank of the Arbuckle Mountains, Oklahoma. The Shale Shaker, 62(4):273–276, 2012.

R. D. Andrews. Cromwell Play in Southeastern Oklahoma. Oklahoma Geological Survey, Oklahoma, United States of America, 2003. ISBN 0275-0929.

F. J. Antinao Fuentealba, J. L. Otegui, and G. L. Bianchi. Improved technique for toughness testing of shale rocks. Engineering Fracture Mechanics, 235(107182):1–13, 2020. doi: 10.1016/j.engfracmech.2020.107182.

B. Bai, M. Elgmati, H. Zhang, and M. Wei. Rock characterization of Fayetteville shale gas plays. Fuel, 105:645–652, 2013. doi: 10.1016/j.fuel.2012.09.043.

R. J. Bodnar and M. L. Frezzotti. Microscale Chemistry: Raman Analysis of Fluid and Melt Inclusions. Elements, 16(2):9398, 2020. doi: 10.2138/gselements.16.2.93.

C. Boyer, B. Clark, V. Jochen, R. Lewis, and C. K. Miller. Shale Gas:A Global Resource. Oilfield Review, 23(3):297–308, 2011.

K. Briggs, A. D. Hill, D. Zhu, and K. Olson. The Relationship Between Rock Properties and Fracture Conductivity in the Fayetteville Shale. pages 1–16. Paper presented at the SPE Annual Technical Conference and Exhibition, Amsterdam, The Netherlands, October 2014, 2014.

A. Busch, S. Alles, Y. Gensterblum, D. Prinz, D. N. Dewhurst, M. D. Raven, H. Stanjek, and B. M. Krooss. Carbon dioxide storage potential of shales. International Journal of Greenhouse Gas Control, 2(3): 297–308, 2008. doi: 10.1016/j.ijggc.2008.03.003.

M. Chen, J. Zhu, H. Zhan, Z. Meng, S. Zhang, R. Chen, K. Zhao, and W. Yue. Direct Detection of Oil Shale Yields: A Laser-Induced Voltage Investigation. Energy & Fuels, 33(2):10691073, 2019. doi: 10.1021/acs.energyfuels.8b04104.

C. R. Clarkson, N. Solano, R. M. Bustin, A. Bustin, G. Chalmers, L. He, Y. B. Melnichenko, A. Radlinski, and T. P. Blach. Pore structure characterization of North American shale gas reservoirs using USANS/SANS, gas adsorption, and mercury intrusion. Fuel, pages 1–29, 2013. doi: 10.1016/j.fuel.2012.06.119.

D. Crandall, J. Moore, M. Gill, and M. Stadelman. CT scanning and flow measurements of shale fractures after multiple shearing events. International Journal of Rock Mechanics and Mining Sciences, 100:177–187, 2017. doi: 10.1016/j.ijrmms.2017.10.016.

D. Davudov, R. G. Moghanloo, and Y. Zhang. Interplay between pore connectivity and permeability in shale sample. International Journal of Coal Geology, 220:103427, 2020. doi: 10.1016/j.coal.2020.103427.

H. Du, M. Radonjic, and Y. Chen. Microstructure and micro-geomechanics evaluation of Pottsville and Marcellus shales. Journal of Petroleum Science and Engineering, 195(107876):1–12, 2020. doi: 10.1016/j.petrol.2020.107876.

A. Duffy, M. Hand, R. Wiser, E. Lantz, A. D. Riva, V. Berkhout, M. Stenkvist, D. Weir, and R. Lacal-Arntegui. Land-based wind energy cost trends in Germany, Denmark, Ireland, Norway, Sweden and the United States. Applied Energy, 277:114777, 2020. doi: 10.1016/j.apenergy.2020.114777.

E. Fjaer, R. Holt, P. Horsrud, A. Raaen, and R. Risnes. Petroleum Related Rock Mechanics. Elsevier, SINTEF Petroleum Research and Norwegian University of Science & Technology, Trondheim, Norway, 2008. ISBN 9780444502605.

F. Foucher, G. Guimbretire, N. Bost, and F. Westall. Petrographical and Mineralogical Applications of Raman Mapping. Raman Spectroscopy and Applications, pages 163–180, 2017. doi: 10.5772/65112.

S. Gao, D. Dong, K. Tao, W. Guo, X. Li, and S. Zhang. Experiences and lessons learned from China's shale gas development: 2005-2019. Journal of Natural Gas Science and Engineering, (103648):1–26, 2020. doi: 10.1016/j.jngse.2020.103648.

Z. Gao and Q. Hu. Wettability of Mississippian Barnett Shale samples at different depths: Investigations from directional spontaneous imbibition. AAPG Bulletin, 100(1):101–114, 2016. doi: 10.1306/09141514095.

G. H. Girty. The fauna of the Caney shale of Oklahoma: Publised by the United States Geological Survey:Bulletin 377. https://doi.org/10.3133/b377, 1909. Online; last accessed October, 2020.

J. Goral, M. Deo, J. McLennan, H. Huang, and E. Mattson. Macro- and micro-compression testing of shales. Journal of Petroleum Science and Engineering, (107034):1–12, 2020. doi: 10.1016/j.petrol.2020.107034.

K. M. Guan, C. M. Ross, and A. R. Kovscek. Multimodal Visualization of Vaca Muerta Shale Fabric Before and After Maturation. Energy & Fuels, 35(11):9550–9560, 2021. doi: 10.1021/acs.energyfuels.1c00037.

A. B. Hagen and C. Thaulow. Low temperature in-situ micro-compression testing of iron pillars. Materials Science and Engineering: A, 678: 355–364, 2016. doi: 10.1016/j.msea.2016.09.110.

H. He, L. Luo, and K. Senetakis. Effect of normal load and shearing velocity on the interface friction of organic shale Proppant simulant. Tribology International, 144(106119):1–8, 2020. doi: 10.1016/j.triboint.2019.106119.

S. Heng, X. Li, X. Liu, and Y. Chen. Experimental study on the mechanical properties of bedding planes in shale. Journal of Natural Gas Science and Engineering, 76(103161):1–22, 2020. doi: 10.1016/j.jngse.2020.103161.

D. G. Henry, I. Jarvis, G. Gillmore, M. Stephenson, and J. F. Emmings. Assessing low-maturity organic matter in shales using Raman spectroscopy: Effects of sample preparation and operating procedure. International Journal of Coal Geology, 191:135–151, 2018. doi: 10.1016/j.coal.2018.03.005.

R. M. Holt, I. Larsen, E. Fjr, and J. F. Stenebrten. Comparing mechanical and ultrasonic behaviour of a brittle and a ductile shale: Relevance to prediction of borehole stability and verification of shale barriers. Journal of Petroleum Science and Engineering, 187(106746):1–12, 2020. doi: 10.1016/j.petrol.2019.106746.

Z. Hou1, M. Gutierrez, S. Ma, A. Almrabat, and C. Yang. Mechanical Behavior of Shale at Different Strain Rates. Rock Mechanics and Rock Engineering, 52:35313544, 2019. doi: 10.1007/s00603-019-01807-7.

Z. Huang, S. Zhang, R. Yang, X. Wu, R. Li, H. Zhang, and P. Hung. A review of liquid nitrogen fracturing technology. Fuel, 266:1–15, 2020. doi: 10.1016/j.fuel.2020.117040.

B. N. Hupp and J. J. Donovan. Quantitative mineralogy for facies definition in the Marcellus Shale (Appalachian Basin, USA) using XRD-XRF integration. Sedimentary Geology, 371:16–31, 2018. doi: 10.1016/j.sedgeo.2018.04.007.

W. D. Ibanez and A. K. Kronenberg. Experimental deformation of shale: Mechanical properties and microstructural indicators of mechanisms. International Journal of Rock Mechanics and Mining Sciences & Geomechanics Abstracts, 30(7):723–734, 1993. doi: 10.1016/0148-9062(93)90014-5.

C. C. Iferobia and M. Ahmad. A review on the experimental techniques and applications in the geomechanical evaluation of shale gas reservoirs. Journal of Natural Gas Science and Engineering, 74(103090), 2020. doi: 10.1016/j.jngse.2019.103090.

M. A. Islam and P. Skalle. An Experimental Investigation of Shale Mechanical Properties Through Drained and Undrained Test Mechanisms. Rock Mechanics and Rock Engineering, 46:13911413, 2013. doi: 10.1007/s00603-013-0377-8.

Itasca. FLAC3d v5.0, Fast Lagrangian Analysis of Continua in 3 Dimensions. Users Guide, 2011.

M. Josh, L. Esteban, C. D. Piane, J. Sarout, D. Dewhurst, and M. Clennell. Laboratory characterisation of shale properties. Journal of Petroleum Science and Engineering, 88-89:107–124, 2012. doi: 10.1016/j.petrol.2012.01.023.

M. Josh, C. D. Piane, L. Esteban, J. Bourdet, S. Mayo, B. Pejcic, I. Burgar, V. Luzin, M. B. Clennell, and D. N. Dewhurst. Advanced labora-

tory techniques characterising solids, fluids and pores in shales. *Journal of Petroleum Science and Engineering*, 180:932–949, 2019. doi: 10.1016/j.petrol.2019.06.002.

S. Kadoshin, T. Nishiyama, and T. Ito. The trend in current and near future energy consumption from a statistical perspective. *Applied Energy*, 67 (4):407–417, 2000. doi: 10.1016/S0306-2619(00)00033-7.

P. J. Kamann. Surface-to-subsurface Correlation and Lithostratigraphic Framework of the Caney Shale (Including the "mayes" Formation) in Atoka, Coal, Hughes, Johnston, Pittsburg, and Pontotoc Counties, Oklahoma. Master's thesis, Oklahoma State University, Boone Pickens School of Geology 105 Noble Research Center Stillwater, OK 74078, 2006.

S. S. Kasyap and K. Senetakis. Characterization of two types of shale rocks from Guizhou China through micro-indentation, statistical and machine-learning tools. *Journal of Petroleum Science and Engineering*, 208:1–14, 2022. doi: 10.1016/j.petrol.2021.109304.

A. Katende, L. OConnell, A. Rich, J. Rutqvist, and M. Radonjic. A comprehensive review of Proppant embedment in shale reservoirs : Experimentation, modeling and future prospects. *Journal of Natural Gas Science and Engineering*, pages 1–29, 2021. doi: 10.1016/j.jngse.2021. 104143.

H. Liu, P. Bedrikovetsky, Z. Yuan, J. Liu, and Y. Liu. An optimized model of calculating optimal packing ratio for graded proppant placement with consideration of proppant embedment and deformation. *Journal of Petroleum Science and Engineering*, 196:1–11, 2021. doi: 10.1016/j.petrol.2020.107703.

K. Liu, M. Ostadhassan, J. Zhou, T. Gentzis, and R. Rezaee. Nanoscale pore structure characterization of the Bakken shale in the USA. *Fuel*, 209:567–578, 2017. doi: 10.1016/j.fuel.2017.08.034.

R. G. Loucks, R. M. Reed, S. C. Ruppel, and U. Hammes. Spectrum of pore types and networks in mudrocks and a descriptive classification for matrix-related mudrock pores. *AAPG Bulletin*, 96(2):1071 –1098, 2012. doi: 10.1306/08171111061.

G. Lu, D. Crandall, and A. P.Bunger. Observations of breakage for transversely isotropic shale using acoustic emission and X-ray computed tomography: Effect of bedding orientation, pre-existing weaknesses, and pore water. *International Journal of Rock Mechanics and Mining Sciences*, 139:1–11, 2021. doi: 10.1016/j.ijrmms.2021.104650.

M. Lubwama, B. Corcoran, K. V. Rajani, C. S. Wong, J. B. Kirabira, A. Sebbit, K. A. McDonnell, D. Dowling, and K. Sayerse. Raman analysis of DLC and Si-DLC films deposited on nitrile rubber. *Surface and Coatings Technology*, 232:521–527, 2013. doi: 10.1016/j.surfcoat. 2013.06.013.

A. M. Lucier, R. Hoffmann, and L. T. Bryndzia. Evaluation of variable gas saturation on acoustic log data from the Haynesville Shale gas play, NW Louisiana, USA. *The Leading Edge*, 30(3):1–9, 2011. doi: 10.1190/1.3567261.

S. Luo, Y. Lu, Y. Wu, J. Song, D. J. DeGroot, Y. Jin, and G. Zhang. Cross-scale characterization of the elasticity of shales: Statistical nanoindentation and data analytics. *Journal of the Mechanics and Physics of Solids*, 140(103945):1–24, 2020. doi: 10.1016/j.jmps.2020. 103945.

L. Ma, A.-L. Fauchille, M. R. Chandler, P. Dowey, K. G. Taylor, J. Mecklenburgh, and P. D. Lee. In-situ synchrotron characterization of fracture initiation and propagation in shales during indentation. *Energy*, (119161,2020), 2020. doi: 10.1016/j.energy.2020.119161.

D. Martogi and S. Abedi. Indentation Based Method to Determine the Mechanical Properties of Randomly Oriented Rock Cuttings. pages 1–8. 53rd U.S. Rock Mechanics/Geomechanics Symposium, 23-26 June, New York City, New York, 2019. URL https://www.onepetro.org/conference-paper/ARMA-2019-1828.

T. J. Maughan and D. Deming. Gas Occurrence in the Caney Shale, Part 1. *The Shale Shaker*, 57(3):77–89, 2006.

N. Meehan. Improving Peoples Lives: The Case for Hydraulic Fracturing. *Journal of Petroleum Technology*, 68(2):1–3, 2016. doi: 10.2118/0216-0010-JPT.

R. S. Middleton, R. Gupta, J. D. Hyman, and H. S. Viswanathan. The shale gas revolution: Barriers, sustainability, and emerging opportunities. *Applied Energy*, 199(1):88–95, 2017. doi: 10.1016/j.apenergy. 2017.04.034.

A. Minardi, S. B. Giger, R. T. Ewy, R. Stankovic, J. Stenebrten, M. Soldal, M. Rosone, A. Ferrari, and L. Laloui. Benchmark study of undrained triaxial testing of Opalinus Clay shale: Results and implications for robust testing. *Geomechanics for Energy and the Environment*, 25:1–17,

2021. doi: 10.1016/j.gete.2020.100210.

S. Mohr, J. Wang, G. Ellem, J. Ward, and D. Giurco. Projection of world fossil fuels by country. *Fuel*, 141(1):120–135, 2015. doi: 10.1016/j.fuel.2014.10.030.

M. Mueller and M. Amro. Indentaion Hardness for Improved Proppant Embedment Prediction in Shale Formations. pages 1–14. SPE European Formation Damage Conference and Exhibition, 3-5 June, Budapest, Hungary, Society of Petroleum Engineers, 2015. doi: 10.2118/174227-MS.

A. Mwesigye and I. H. Yilmaz. Thermal and thermodynamic benchmarking of liquid heat transfer fluids in a high concentration ratio parabolic trough solar collector system. *Journal of Molecular Liquids*, pages 1–21, 2021. doi: 10.1016/j.molliq.2020.114151.

S. Nakagawa and E. Borglin. Laboratory In-Situ Visualization of Long-Term Fracture Closure and Proppant Embedment in Brittle and Ductile Shale Samples. pages 1–8. 53rd US Rock Mechanics/Geomechanics Symposium held in New York, NY, USA, 2326 June 2019, 2019.

W. Oliver and G. Pharr. An improved technique for determining hardness and elastic modulus using load and displacement sensing indentation experiments. *Journal of Materials Research*, 7(6):1564 – 1583, 1992. doi: 10.1557/JMR.1992.1564.

R. W. Pachytel, M. Jarosinski, and K. Bobek. Geomechanical Stratification in a Shale Reservoir and Its Correlation With Natural Fractures: Case From Pomeranian Basin (Poland). pages 1–10. 51st U.S. Rock Mechanics/Geomechanics Symposium, 25-28 June, San Francisco, California, USA, 2017.

K. Pruess, C. Oldenburg, and G. Moridis. Report LBNL-43134. Lawrence Berkeley National Laboratory, Berkeley, CA, USA. *Users Guide 2.1*, 2012.

M. Radonjic, G. Luo, Y. Wang, M. Achang, J. Cains, A. Katende, J. Puckette, M. Grammer, and G. E. King. Integrated Microstructural Characterisation of Caney Shale, OK. pages 1–18. Unconventional Resources Technology Conference, 2020. doi: 10.15530/urtec-2020-2947.

J. Rutqvist. An overview of TOUGH-based geomechanics models. *Computers & Geosciences*, 108:56–63, 2017. doi: 10.1016/j.cageo.2016.09. 007.

T. Saif, Q. Lin, A. R.Butcher, B. Bijeljic, and M. J. Blunt. Multi-scale multi-dimensional microstructure imaging of oil shale pyrolysis using X-ray micro-tomography, automated ultra-high resolution SEM, MAPS Mineralogy and FIB-SEM. *Applied Energy*, 202:628–647, 2017. doi: 10.1016/j.apenergy.2017.05.039.

A. Sarycheva and Y. Gogotsi. Raman Spectroscopy Analysis of the Structure and Surface Chemistry of Ti3C2Tx MXene. *Chemistry of Materials*, 32(8):3480–3488, 2020. doi: 10.1021/acs.chemmater.0c00359.

S. T. Schad. Hydrocarbon Potential of the Caney Shale in Southeastern Oklahoma. Master's thesis, The University of Tulsa, College of Engineering and Natural Sciences 800 S. Tucker Drive Tulsa, OK 74104, 2004.

V. Sharma and A. Sircar. Multi-technique characterization of shale reservoir quality parameters. *Journal of Natural Gas Science and Engineering*, 103125,2020, 2020. doi: 10.1016/j.jngse.2019.103125.

S. A. Solarin and M. O. Bello. The impact of shale gas development on the U.S economy: Evidence from a quantile autoregressive distributed lag model. *Energy*, 15(118004):1–10, 2020. doi: 10.1016/j.energy.2020. 118004.

H. Sone and M. D. Zoback. Mechanical properties of shale-gas reservoir rocks Part 1: Static and dynamic elastic properties and anisotropy. *Geophysics*, 78(5):1942–2156, 2013a. doi: 10.1190/geo2013-0050.1.

H. Sone and M. D. Zoback. Mechanical properties of shale-gas reservoir rocks Part 2: Ductile creep, brittle strength, and their relation to the elastic modulus. *Geophysics*, 78(5):1942–2156, 2013b. doi: 10.1190/geo2013-0051.1.

P. Stemmermann, K. Garbev, B. Gasharova, G. Beuchle, M. Haist, and T. Divoux. Chemo-mechanical characterization of hydrated calcium-hydrosilicates with coupled Raman- and nanoindentation measurements. *Applied Geochemistry*, 118(104582):1–10, 2020. doi: 10.1016/ j.apgeochem.2020.104582.

M. Sun, J. Zhao, Z. Pan, Q. Hu, B. Yu, Y. Tan, L. Sun, L. Bai, C. Wu, T. P. Blach, Y. Zhang, C. Zhang, and G. Cheng. Pore characterization of shales: A review of small angle scattering technique. *Journal of Natural Gas Science and Engineering*, 78(103294), 2020. doi: 10.1016/j.jngse.2020.103294.

J. A. Taff. Description of the Coalgate Quadrangle: Published by the United

States Geological Survey. https://pubs.usgs.gov/gf/074/text.pdf, 1901. Online; last accessed October, 2020.

B. P. Tissot and D. H. Welte. *Petroleum Formation and Occurrence*. Springer, 1978. ISBN 978-3-642-96446-6.

H. S. Truong-Lam, S. J. Cho, and J. D. Lee. Simultaneous in-situ macro and microscopic observation of CH4 hydrate formation/decomposition and solubility behavior using Raman spectroscopy. *Applied Energy*, 255(113834):1–9, 2020. doi: 10.1016/j.apenergy.2019.113834.

G. Turrell and J. Corset. *Raman Microscopy: Developments and Applications*. Elsevier, Universite des Sciences et Technologies de Lille Villeneuve d'Ascq, France, & Laboratoire de Spectrochimie Infraruge et Raman (CNRS UPR A2631T) 2 rue Henri-Dunant, 94320 Thiais, France, 1996. ISBN 978-0-12-189690-4.

D. Tuschel. Raman Spectroscopy of Oil Shale. *Spectroscopy*, 28(3):1–6, 2013.

M. Voltolini and J. Ajo-Franklin. Evolution of propped fractures in shales: The microscale controlling factors as revealed by in situ X-Ray microtomography. *Journal of Petroleum Science and Engineering*, 188 (106861):1–11, 2020. doi: 10.1016/j.petrol.2019.106861.

M. Voltolini, J. Rutqvist, and T. Kneafsey. Coupling dynamic in situ X-ray micro-imaging and indentation: A novel approach to evaluate micromechanics applied to oil shale. *Fuel*, 300:1–12, 2021. doi: 10.1016/j.fuel.2021.120987.

T. Vulgamore, S. Wolhart, M. Mayerhofer, T. Clawson, and C. Pope. . Hydraulic Fracture Diagnostics Help Optimize Stimulations Of Woodford Shale Horizontals. *The America Oil&Gas Reporter*, 2008.

X. Wang, J. Hou, S. Li, L. Dou, S. Song, Q. Kang, and D. Wang. Insight into the nanoscale pore structure of organic-rich shales in the Bakken Formation, USA. *Journal of Petroleum Science and Engineering*, 191: 1–9, 2020. doi: 10.1016/j.petrol.2020.107182.

G. A. Yakaboylu, N. Gupta, E. M. Sabolsky, and B. Mishra. Mineralogical characterization and macro/microstrain analysis of the Marcellus shales. *International Journal of Rock Mechanics and Mining Sciences*, 134:1–12, 2020. doi: 10.1016/j.ijrmms.2020.104442.

S. C. D. Yin, N. Jiang, F. Wang, and Z. Zhao. Mechanical properties of oil shale-coal composite samples. *International Journal of Rock Mechanics and Mining Sciences*, 123(104120):1–10, 2019. doi: 10.1016/j.ijrmms.2019.104120.

J. Yuan, D. Luo, and L. Feng. A review of the technical and economic evaluation techniques for shale gas development. *Applied Energy*, 148: 49–65, 2015. doi: 10.1016/j.apenergy.2015.03.040.

Y. Zhang, M. Lebedev, A. Al-Yaseri, H. Yu, X. Xu, M. Sarmadivaleh, A. Barifcani, and S. Iglauer. Nanoscale rock mechanical property changes in heterogeneous coal after water adsorption. *Fuel*, 218:23–32, 2018. doi: 10.1016/j.fuel.2018.01.006.

S. Zhi and D. Elsworth. Proppant embedment in coal and shale: Impacts of stress hardening and sorption. *International Journal of Coal Geology*, (103545,2020), 2020. doi: 10.1016/j.coal.2020.103545.

Z. Zong, J. Lou, O. Adewoye, A. Elmustafa, F. Hammad, and W. Soboyejo. Indentation size effects in the nano- and micro-hardness of fcc single crystal metals. *Materials Science and Engineering: A*, 434:178–187, 2006. doi: 10.1016/j.msea.2006.06.137.